Modeling Stochastic Conditional Dynamics from Sparse Observations via Kernel-Stabilized Flow Matching

Anonymous authors
Paper under double-blind review

Abstract

Learning to transform conditional probability densities over time is a fundamental challenge spanning probabilistic modeling and the natural sciences. This task is paramount when forecasting the evolution of stochastic nonlinear dynamical systems in biological and physical domains. While flow-based models can predict the temporal evolution of probability distributions, existing approaches often assume discrete conditioning with samples that are paired across time, limiting their scientific applicability where frequently only sparse data with unpaired continuous conditioning is available. We propose *Conditional Variable Flow Matching* (CVFM), a framework for learning flows transforming conditional distributions with amortization across the continuous space of conditional densities. CVFM addresses the high-variance instability of prior methods by jointly sampling flows over state and conditioning variables, utilizing a conditioning mismatch kernel alongside a conditional Wasserstein distance to reweight the conditional optimal transport objective. Collectively, these advances allow for learning dynamics from sparse unpaired measurements of state-condition across time. We evaluate CVFM on conditional mapping benchmarks and a case study modeling the temporal evolution of materials internal structure during manufacturing processes, observing improved performance and convergence characteristics over existing conditional variants.

1 Introduction

Appropriately modeling the time-dependent evolution of distributions is a central goal in multiple scientific fields, such as single-cell genomics (Tong et al., 2023a; Bunne et al., 2023a), meteorology (Fisher et al., 2009), robotics (Ruiz-Balet & Zuazua, 2023; Chen et al., 2021), and materials science (Kalidindi, 2015; Adams et al., 2013). Across the sciences, forecasting stochastic nonlinear dynamical systems requires a methodology for learning the transformations of time-evolving densities. For many applications, this capability must be achievable given only *unpaired* observational samples[1], or observations across time which are not in correspondence. This requirement arises due to practical constraints on data collection in such applications. For example, in both single-cell genomics and materials science, experimental testing to quantify the system's state is often destructive, precluding measurement of the state of a single sample across multiple time steps (Tong et al., 2023a; Bunne et al., 2023a; Ghanavati & Naffakh-Moosavy, 2021; ASTM International, 2024).

Various approaches to address this challenge have recently been proposed, including diffusion Schrödinger bridges (DSB) (Liu et al., 2022a; Chen et al., 2023; De Bortoli et al., 2021; Bunne et al., 2023a; Tang et al., 2024) alongside extensions of Flow Matching (FM) (Tong et al., 2023b;a). These approaches generalize denoising diffusion probabilistic models (Ho et al., 2020), score matching (Song et al., 2021), and FM (Lipman et al., 2023; Albergo & Vanden-Eijnden, 2023; Liu et al., 2022b), to arbitrary source distributions – a

[1]For unconditioned distributions, *unpaired* samples refers to the ability to sample from time marginal distributions independently, $x_0 \sim p_0(x)$ and $x_1 \sim p_1(x)$, rather than the joint, $p(x_0, x_1)$.

necessary relaxation to model the evolutionary pathways of physical or biological systems, as such natural systems rarely exhibit Gaussian source distributions[2].

Despite the apparent success of such approaches, their practical utility has been limited, as they solely permit the simulation of evolving unconditional distributions. However, in modeling the dynamics of real systems, the most critical questions often take the form of *how might an intervention affect the resulting dynamics*? For example, the dynamics of materials manufacturing processes depend upon process parameters such as applied temperature or power (Liu et al., 2022c; Schrader & Elshennawy, 2000). Such questions require modeling the evolution of conditional distributions. Once more, we are restricted by our limited ability to observe their time-dependent states. In addition to unpaired state measurements, we often face the challenge of unpaired conditioning, which we define as the scenario in which data observed at discrete time frames possesses conditioning variables which are similarly unpaired. Formally, observed samples are drawn independently from their respective joint distributions at the initial and final time steps[3] as $(x_0, y_0) \sim p_0(x, y), (x_1, y_1) \sim p_1(x, y)$ where there is no guarantee that $y_0 = y_1$, distinguishing this from traditional conditional settings where a fixed y is observed. Aside from the destructive nature of common data collection in the sciences, unpaired conditioning commonly arises due to the prohibitive costs of sample acquisition. Design-of-experiments or active learning approaches are frequently employed to mitigate these costs by minimizing the number of experiments – identifying a series of maximally informative test configurations (Lookman et al., 2019; Tran et al., 2020). This diversity ensures that conditioning is purposefully rarely repeated.

Extensions modeling the dynamics of conditional distributions are rapidly developing (Ho & Salimans, 2022; Zheng et al., 2023; Bunne et al., 2022; Harsanyi et al., 2024; Bunne et al., 2023b; Isobe et al., 2024). Conditional input convex neural networks (ICNN) (Bunne et al., 2022; Harsanyi et al., 2024; Bunne et al., 2023b) and initial conditional extensions of flow matching (Isobe et al., 2024; Zheng et al., 2023; Dao et al., 2023), in particular, require datasets with matching conditioning, or the ability to first be able to select $y \in \mathcal{Y}$ and subsequently sample $x_t \sim p_t(x|y)$. This structure degrades in the limit of continuous conditioning variables, where obtaining multimarginal samples with equivalent conditioning is infeasible. While select recent works have begun to explore extensions enabling such continuous conditional treatment through conditional optimal transport (OT) between densities, these formulations suffer from high-variance instabilities (Chemseddine et al., 2024; Kerrigan et al., 2024; Baptista et al., 2024; Tabak et al., 2019). We demonstrate that in sparse data regimes – common in scientific discovery – standard mini-batch approximations of the conditional coupling lead to variance explosion, rendering training unstable or non-convergent. To address this, we introduce a conditioning mismatch kernel which explicitly enforces local consistency on the conditioning manifold. This addition coupled with the conditional Wasserstein distance, combine to significantly increase the algorithms' stability and performance.

We propose *Conditional Variable Flow Matching* (CVFM), a general approach for learning the flow between source and target conditional distributions. Importantly, CVFM supports *entirely unpaired datasets*, wherein neither the sample data nor their corresponding conditioning variables need to be paired. We motivate the proposed CVFM algorithm through a theoretical analysis of the stability of flow matching on conditional densities, formally establishing the conditional identity coupling as a prerequisite for consistent vector field learning. To address this, core to CVFM is the usage of two conditional flows, a conditional Wasserstein distance, and a condition-dependent mismatch kernel, generalizing and stabilizing existing simulation-free objectives for continuous normalizing flows (CNF) (Lipman et al., 2023; Albergo & Vanden-Eijnden, 2023) and stochastic dynamics (Tong et al., 2023a; Shi et al., 2023) to the conditional setting. We specifically focus on dynamics wherein the marginal distribution over the conditioning variable remains constant – a common setting in applied problems. The algorithm is introduced in the dynamical formulation of optimal transport (OT), augmenting FM and ordinary differential equation (ODE) based transport in defining a straightforward training objective for learning amortized conditional vector fields. Our objective facilitates simulation across the conditional density manifold, leveraging these mechanisms to

[2]We note that when approximating the dynamics of real systems, the model is trained to transform the state density between successive time steps. Therefore, even if the density at $t = 0$ is Gaussian, the bridge between arbitrary time steps must be generalized.

[3]These times can be fictitious (as in standard generative models, (Tong et al., 2023b)) or can refer to the real time between time steps (as in dynamics, (Tong et al., 2023a)).

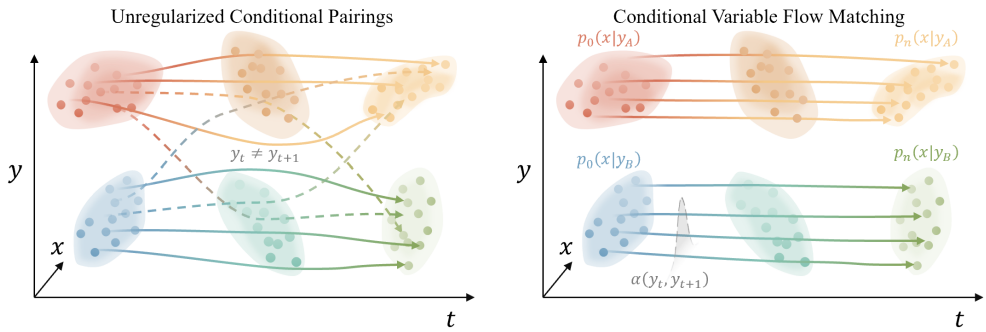

Figure 1. **The stability gap in learning conditional dynamics from unpaired data. (Left) Unregularized Conditional Pairings:** Standard conditional flow matching methods employ couplings (such as naive or conditional OT $\pi_\eta((x, y), (x', y'))$) that **generate pairings without enforcing local conditional consistency**. In sparse data regimes, these unregularized couplings often propose pairings between samples with disparate conditioning values (e.g., coupling $p(x|y_A)$ to $p(x|y_B)$ where y_A, y_B denote conditioning variables drawn from disjoint subsets $\mathcal{Y}_A, \mathcal{Y}_B \subset \mathcal{Y}$). This results in high-variance, mismatched flows where the dynamics erroneously jump across the conditioning manifold ($y_t \neq y_{t+1}$). **(Right) Conditional Variable Flow Matching (CVFM):** Our framework integrates a conditioning mismatch kernel $\alpha(y_t, y_{t+1})$ with the conditional Wasserstein distance in the training objective. The kernel acts as a soft filter, suppressing the mismatched trajectories proposed by the OT solver while retaining locally consistent pairings. The result is a conditionally stable, laminar vector field that respects the underlying conditional distributions.

enable robust conditional OT. Subsequently, we analyze CVFM on several toy problems, demonstrating its superior performance and convergence behavior compared to existing methods. The performance of CVFM is further demonstrated in two more challenging case studies: the high-dimensional dynamics of material microstructure evolution conditioned on various manufacturing processes, and class conditional image-to-image mapping. As a part of these latter case studies, we further demonstrate the applicability of our method to approximating conditional Schrödinger bridges with a score-based stochastic differential equation (SDE) extension to FM (Tong et al., 2023a).

2 Dynamic Mass Transport Methods

2.1 Flow Matching

Continuous Normalizing Flows (CNF) (Chen et al., 2018) define a mapping between distributions $x_0 \sim p_0(x)$ and $x_1 \sim p_1(x)$ on the same domain, $x_0, x_1 \in \mathbb{R}^N$ via the following ordinary differential equation (ODE).

$$\frac{d}{dt}\phi_t(x) = u_t(\phi_t(x)), \quad \phi_0(x) = x \tag{1}$$

Individual samples $x_0 \sim p_0(x)$ can be transformed to $x_1 \sim p_1(x)$ by integrating the vector field $u_t : [0, 1] \times \mathbb{R}^N \to \mathbb{R}^N$ and solving the ODE in Eq. (1).

Flow matching (FM) provides a simulation-free objective for constructing the *marginal probability path* $p_t(x)$ via a marginalization of sample conditioned probability paths $p_t(x|z)$, conditioned on observations $z = (x_0, x_1)$ drawn from the empirical distributions – distributions defined implicitly by a set of observed data at the initial and final time steps, $q(x_0)$ and $q(x_1)$. Lipman et al. (2023) demonstrates that one can similarly marginalize over conditional vector fields $u_t(x|z)$ to construct $u_t(x)$, generating the probability flow $p_t(x)$ (Theorem 1 (Lipman et al., 2023)). The consequences of which permit directly regressing upon the conditional vector field as

$$\mathcal{L}_{\text{CFM}}(\theta) = \mathbb{E}_{t,q(z),p_t(x|z)}\|v_\theta(x, t) - u_t(x|z)\|^2 \tag{2}$$

where for conditional Gaussian paths $p_t(x|z) = \mathcal{N}(x|\mu_t(z), \sigma_t^2(z))$ of $\phi_{t,z}(x) = \mu_t(z) + \sigma_t(z)x$ the unique conditional vector field $u_t(x|z)$ can be solved in closed form (Theorem 3 (Lipman et al., 2023), Theorem 2.1, (Albergo & Vanden-Eijnden, 2023)).

2.2 Optimal Transport

The optimal transport (OT) problem aims to identify a mapping between measures, ν and μ, with minimal displacement cost (Villani, 2009). The Kantorovich relaxation attempts to recover the OT coupling π given the potential set of all couplings on $\mathbb{R}^N \times \mathbb{R}^N$, such that the coupling's marginals are the original distributions, $\Pi(\mu, \nu) = \{\pi \in \mathcal{P}(\mathcal{X} \times \mathcal{Y}) : P_{\mathcal{X}\#}\pi = \mu \text{ and } P_{\mathcal{Y}\#}\pi = \nu\}$. The resulting distance $W(\mu, \nu)$ is the Wasserstein distance

$$W(\mu, \nu) = \inf_{\pi \in \Pi(\mu,\nu)} \int c(x, y)\pi(x, y)dxdy \tag{3}$$

where the squared Wasserstein-2 distance $W(\mu, \nu)_2^2$ is induced by the ground cost $c(x, y)^2$.

Entropically-Regularized OT: OT can be made computationally efficient by adding a KL penalty between the coupling π and the independent joint $\mu \otimes \nu$, leading to the Sinkhorn formulation (Cuturi, 2013).

OT-FM: While the Gaussian conditional probability paths for $p_t(x|z)$ in FM are the OT paths after conditioning on z (Peyré & Cuturi, 2020), the induced marginal flow, defining $p_t(x)$, does not provide OT between distributions. Recent works have demonstrated that approximate *dynamic* marginal OT can be achieved through identifying the *static* OT map within mini-batches, and resampling $q(z) = \pi^*(x_0, x_1)$ according to the OT coupling π^*(Tong et al., 2023b; Pooladian et al., 2023).

2.3 Schrödinger Bridge

The Schrödinger bridge problem aims to identify the most likely stochastic mapping between arbitrary marginal distributions $\mathbb{P}_0 = \mu_0$ and $\mathbb{P}_1 = \mu_1$ with respect to a given reference process $\mathbb{Q}$ (Cuturi, 2013; Léonard, 2013; Schrödinger, 1932), defined as $\mathbb{P}_t^* = \text{argmin}_{\mathbb{P}_0=\mu_0,\mathbb{P}_1=\mu_1} \text{KL}(\mathbb{P}_t \| \mathbb{Q}_t)$. Frequently, $\mathbb{Q}$ is taken to be $\mathbb{Q} = \sigma\mathbb{W}$, where $\mathbb{W}$ is standard Brownian motion, otherwise known as the *diffusion Schrödinger bridge* (De Bortoli et al., 2021; Chen et al., 2022; Vargas, 2021; Bunne et al., 2023a; Shi et al., 2023).

Prior work has elucidated a rich relationship between the Schrödinger bridge problem and OT, in particular entropy-regularized OT (Léonard, 2013; Mikami & Thieullen, 2006; Mikami, 2004; Léonard, 2010). More specifically, with the reference process assumed as standard Brownian motion, the marginals of the dynamic Schrödinger bridge can be considered to be a mixture of Brownian bridges weighted by the *static* entropic OT coupling, a construction reminiscent to the marginalization of probability paths in FM (Léonard, 2010; 2013).

$$p_t(x) = \int p_t(x|z)d\pi_\varepsilon^*(z). \tag{4}$$

2.4 Score and Flow Matching

Given the notable connection between the Schrödinger bridge problem (Schrödinger, 1932) and entropy regularized OT (Léonard, 2013; Mikami & Thieullen, 2006; Mikami, 2004; Léonard, 2010), a natural step to address this challenge in a simulation-free manner is to seek an extension to the OT-FM objective. Tong et al. (2023a) demonstrated the feasibility of this approach through generalizing Eq. (2) to simultaneously regress on the conditional drift and score of an SDE. The proposed method replaces the flow ODE with the general SDE $dx = u_t(x)dt + g(t)dw_t$ where $u_t(x)$ is the SDE drift, dw_t is standard Brownian motion, and $g(t)$ is the diffusion coefficient (Tong et al., 2023a). The SDE drift and a corresponding ODE vector field $\hat{u}_t(x)$ are intimately related by the *probability flow* ODE of the process: $\hat{u}_t(x) = u_t(x) - \frac{g(t)^2}{2}\nabla \log p_t(x)$.

Mirroring the previous flow-based models, the vector field, $u_t(x)$, and the score function, $s_t(x) = \nabla \log p_t(x)$, defining the SDE's drift are unknown. Score and Flow Matching ([SF]^{2}M) involves generalizing FM, Eq. (2), to fit approximators of both objects

$$\mathcal{L}_{[\text{SF}]^2\text{M}}(\theta) = \mathcal{L}_{\text{CFM}}(\theta) + \mathbb{E}_{t,q(z),p(x|z)}\lambda(t)^2\|s_\theta(x, t) - \nabla \log p_t(x|z)\|^2 \tag{5}$$

where $\lambda(t)^2$ is a time-dependent normalization factor ensuring uniform weighting of the score across time (Tong et al., 2023a; Song et al., 2021; Ho et al., 2020; Karras et al., 2022). Further background can be found in Appendix B.

We emphasize that the conceptual similarity between the derivation of the flow matching objective and that of generalized score and flow matching signifies that any improvements in the first can be readily transferred to the second. As a result, in this work we theoretically restrict ourselves to purely flow-based models to simplify communication of novel developments, while case studies also include score and flow-based models.

3 Conditional Variable Flow Matching

In the following section, we generalize the FM objective in Eq. (2) to matching the flow between arbitrary conditional distributions, $p_0(x|y)$ to $p_1(x|y)$, provided *unpaired* observations with distinct conditioning variables.

3.1 Constructing Conditional Probability Paths and Vector Fields

We first note that the original marginalization motivating the flow matching objective can be extended to construct a probability flow across both x and a conditioning variable y as

$$p_t(x|y) = \int p_t(x|y, z, w)q(z, w)dzdw \tag{6}$$

where $q(z, w)$ now denotes the empirical distribution over $z = (x_0, x_1)$ and $w = (y_0, y_1)$, where samples are drawn from $x_0, y_0 \sim q(x_0, y_0)$ and $x_1, y_1 \sim q(x_1, y_1)$. We further assume that the conditional joint probability path decomposes as $p_t(x, y|z, w) = p_t(x|z)p_t(y|w)$, resulting in two simultaneous conditional flows, one over the state variable x given marginal observations z, and the other over the conditioning variable y given the associated marginal sampled conditioning variables w. In other words, we assume that the joint distribution at intermediate times, $p_t(x, y)$, retains a dependency between x and y defined by the joint discrete time empirical distributions.

We can also extend this line of thought towards defining a marginal conditional vector field, through marginalizing over vector fields conditioned on observations z and w as

$$u_t(x|y) = \mathbb{E}_{q(z,w)} \frac{u_t(x|z)p_t(x|z)p_t(y|w)}{p_t(x, y)} \tag{7}$$

where $u_t(x|z) : \mathbb{R}^N \to \mathbb{R}^N$ is a conditional vector field generating $p_t(x|z)$ from $p_0(x|z)$, without any explicit dependence upon the conditional distribution over y. Following Theorem 3 (Lipman et al., 2023), Theorem 2.1, (Albergo & Vanden-Eijnden, 2023), and Theorem 3.1 (Tong et al., 2023a), we prescribe a form to both conditional vector fields such that they generate their respective conditional probability distributions[4]. This method of combining conditional vector fields can be shown to generate the marginal conditional vector field, $u_t(x|y)$, which is formalized in the following theorem.

Theorem 3.1 *The marginal conditional vector field Eq. (7) generates the marginal conditional probability path Eq. (6) from $p_0(x|y)$ given samples of $q(z, w)$ if $q(y_0) = q(y_1)$ and the conditioning variable pairs (y_0, y_1) drawn from $q(z, w)$ follow the identity coupling.*

Equality of the empirical distributions refers to equality in the underlying distribution, not the sample sets which define them implicitly. This result deviates from prior results in standard Flow Matching by Lipman et al. (2023) (Theorem 1) and Albergo et al. (2023) (Theorem 2.6) as well as recent concurrent studies in flow matching for conditional densities (Kerrigan et al., 2024); the theorem states that optimal transport over the conditioning variable is necessary for learning amortized conditional vector fields. Our framework is

[4]For Gaussian probability paths with deterministic dynamics: $u_t(x|z) = x_1 - x_0$ (Pooladian et al., 2023; Tong et al., 2023b; Albergo & Vanden-Eijnden, 2023) and stochastic dynamics: $\hat{u}_t(x|z) = ((1 - 2t)/(2t(1 - t)))(x - (tx_1 + (1 - t)x_0)) + (x_1 - x_0)$, $\nabla_x \log p_t(x|z) = (tx_1 + (1 - t)x_0 - x)/(\sigma^2 t(1 - t))$ (Tong et al., 2023a).

designed specifically to implement this conclusion. Through this lens, we will see the practical implications on learned mappings and training dynamics when this result is violated. The full proof of all theorems are provided in Appendix A.

3.2 Flow Matching for Conditional Distributions

Even given Eq. (6) and Eq. (7), their incorporation in an overall objective for training a neural network approximator to $u_t(x|y)$ is still limited by several intractable integrals. Instead, we can obtain an unbiased estimator of the marginal conditional vector field and resulting probability path provided only samples from known distributions and the ability to compute $u_t(x|z)$ through the proposed conditional variable flow matching objective.

$$\mathcal{L}_{\text{CVFM}}(\theta) = \mathbb{E}_{t,q(z,w),p_t(x|z)p_t(y|w)}\left[\alpha(w)\|v_\theta(x,y,t) - u_t(x|z)\|^2\right] \tag{8}$$

The conditioning mismatch kernel $\alpha(w)$ dynamically modulates the acceptance of conditioning pairs, further facilitating conditional OT. The following theorem formalizes the use of the tractable objective in Eq. (8) as a close approximation to the ideal marginal objective.

Theorem 3.2 *Let $p_t(x|y) > 0$ for all $x \in \mathbb{R}^N$, $y \in \mathbb{R}^M$, $t \in [0,1]$ and $\mathcal{L}_{MCFM}(\theta) = \mathbb{E}_{t,p_t(x,y)}\|v_\theta(x,y,t) - u_t(x|y)\|_2^2$. Let α be a stationary, isotropic kernel depending only on $w = \|y_0 - y_1\|_2$, decaying to 0 as $w \to \infty$, and $\mathcal{C}^2$ in a neighborhood of 0 with $\alpha(0) = 1$ and $\alpha'(0) = 0$, and further assume the coupling $\pi(w)$ satisfies $\mathbb{E}_{\pi(w)}[\|y_0 - y_1\|_2^2] < \infty$. Then there exists a constant C such that for every θ,*

$$\left\|\nabla_\theta \mathcal{L}_{\text{CVFM}}(\theta) - \nabla_\theta \mathcal{L}_{\text{MCFM}}(\theta)\right\| \leq C\,\mathbb{E}\left[\|y_0 - y_1\|^2\right]. \tag{9}$$

If $\pi(w)$ enforces $\mathbb{E}_{\pi(w)}[\|y_0 - y_1\|_2^2] = O(\varepsilon^2)$ then the gradient error is $O(\varepsilon^2)$.

3.3 Stabilizing and Accelerating Training

Unlike previous flow matching frameworks, the empirical distribution, $q(z,w)$, cannot be sampled arbitrarily (Lipman et al., 2023; Tong et al., 2023a). Samples must be drawn such that $w = (y_0, y_1)$ follows the identity coupling $\pi(y_0, y_1)$, the theoretical reasons for which are described in Appendix A. We introduce two components to achieve this: an anisotropic transport cost, and a conditioning mismatch kernel.

Anisotropic Optimal Transport for Conditional Distributions: We consider two probability distributions, a source μ and a target ν, in the space $\mathcal{P}(\mathcal{X} \times \mathcal{Y})$, where $\mathcal{X} \subseteq \mathbb{R}^N$ and $\mathcal{Y} \subseteq \mathbb{R}^M$. We aim to find an OT plan $\pi \in \Pi(\mu, \nu)$ that primarily transports mass along the $\mathcal{X}$ dimension while penalizing transport along the $\mathcal{Y}$ dimension.

A hard constraint forbidding transport in $\mathcal{Y}$ would require that for any pair of coupled points $((x,y),(x',y'))$ in the support of π, we must have $y = y'$. This is often infeasible, especially in the empirical setting with continuous data. Instead, we introduce a penalty into the ground cost, an approach also explored in concurrent work (Kerrigan et al., 2024; Chemseddine et al., 2024; Baptista et al., 2024). We define the anisotropic cost function $c_\eta : (\mathcal{X} \times \mathcal{Y})^2 \to \mathcal{R}^+$ as:

$$c_\eta((x,y),(x',y')) = \|x - x'\|_p + \eta\|y - y'\|_p \tag{10}$$

where $\eta > 0$ is a hyperparameter controlling the penalty for transport in $\mathcal{Y}$, and $\|x\|_p$ is the p-norm. In this context, we refer to the transport cost induced by this anisotropic ground cost c_η as the conditional Wasserstein distance.

Proposition 3.1 *Let $\mu, \nu \in \mathcal{P}(\mathbb{R}^N \times \mathbb{R}^M)$ have finite p-th moments, and let $\mu_\mathcal{Y}$ and $\nu_\mathcal{Y}$ be their respective marginal distributions on $\mathbb{R}^M$. Let π_η be an OT plan for the cost c_η in Eq. (10). In the limit as the penalty parameter grows, the expected transport cost in the $\mathcal{Y}$ dimension converges to the p-Wasserstein distance between the marginals:*

$$\lim_{\eta\to\infty} \mathbb{E}_{((x,y),(x',y'))\sim\pi_\eta}[\|y - y'\|_p] = W_p(\mu_\mathcal{Y}, \nu_\mathcal{Y}) \tag{11}$$

If the marginals are identical ($\mu_\mathcal{Y}$=$\nu_\mathcal{Y}$), then this limit is zero.

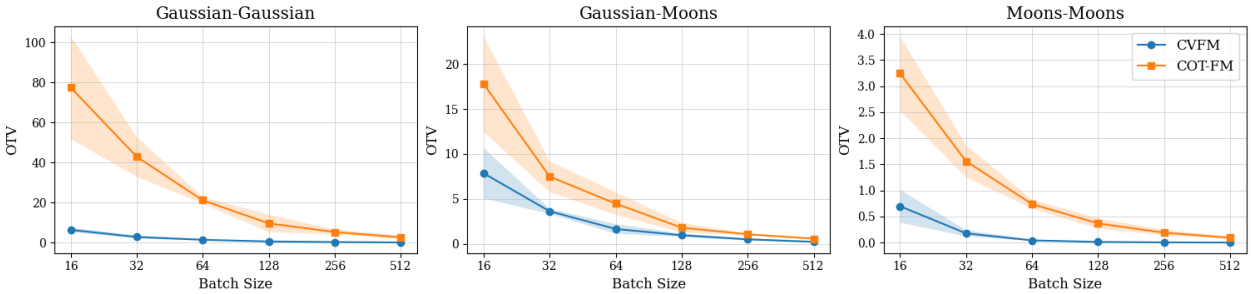

Figure 2. Impact of the kernel $\alpha(w)$ on estimator stability. Comparison of Objective Target Variance (OTV) across batch sizes for CVFM and COT-FM Kerrigan et al. (2024); Chemseddine et al. (2024). COT-FM exhibits explosive variance in sparse data regimes ($B = 16$). CVFM effectively suppresses this variance in all cases, demonstrating that the kernel is essential for stable training when dense sampling of the conditioning manifold is infeasible. Values were computed with $\eta = 10$ over 5 seeds and are shown as $\mu \pm \sigma$.

In practice, we approximate the OT plan using mini-batches. In each iteration, we draw k samples $(x_i, y_i)_{i=1}^k$ from the source μ and k samples $(x'_j, y'_j)_{j=1}^k$ from the target ν, forming empirical measures μ^k and ν^k. The coupling is then estimated by solving the discrete OT problem between μ^k and ν^k with the cost c_η.

Conditioning Mismatch Kernel: While mini-batch OT approximates the correct coupling, it introduces significant estimator variance in regimes where the conditioning manifold is sparse. In such cases, samples with disparate conditioning values are paired, leading to noisy high-cost pairings which destabilize the vector field regression in Eq. (2). To mitigate this, CVFM incorporates a dynamic scaling term in the form of a stationary symmetric kernel $\alpha(w)$ into the objective (Eq. (8)). This term acts as a variance reduction mechanism by modulating the loss based on the degree of mismatch in the sampled conditioning variables (y_0, y_1), effectively suppressing the contribution of mismatched pairings and promoting the conditional identity coupling, see Appendix E.2 for analysis. CVFM utilizes a squared exponential kernel, $\alpha(w) = \exp(-\|y_0 - y_1\|_2^2/2\sigma_y^2)$; however, our framework supports any stationary, positive-definite kernel that is a monotonically decreasing function of $\|y_0 - y_1\|_p$ (see Appendix E.2). As demonstrated in the following analysis, the kernel's presence stabilizes training – combating the need for long training schemes commonly required for flow matching methods – and improves overall performance. In particular, this addition is critical for ensuring model performance and training stability in sparse data regimes frequently encountered in scientific applications.

Motivating Analysis: To explicitly validate this, we analyze the Objective Target Variance (OTV), defined as $\mathbb{E}_{t,q,p_t}||u_t(x|z)||^2$, on a canonical 2D manifold with strong conditional dependence (see *8 Gaussian–8 Gaussian* in Sec. 4). As illustrated in Figure 2, the anisotropic cost function Eq. (10) in isolation (COT-FM) exhibits variance explosion when batch sizes are small ($B = 16$), simulating the sparse data availability common in scientific applications. In this regime, the mini-batch OT solver is forced to couple samples with disparate conditioning values ($y \neq y'$) simply to satisfy marginal constraints, creating high-variance target velocities that contradict the local conditional geometry. By incorporating the kernel, CVFM suppresses this variance by an order of magnitude, ensuring stable convergence even when dense sampling of the conditioning variable is infeasible. Further analysis is provided in Appendix E. This empirical observation aligns with our theoretical insight, in COT-FM, the estimator variance scales with the volume of the conditioning space. The kernel effectively reduces the effective sample volume to a local neighborhood, bounding the variance.

4 Experiments

We experimentally evaluate the performance of the proposed CVFM framework in accurately recovering target conditional densities on a suite of increasingly demanding problems. We first interrogate its performance on three 2D toy problems to baseline CVFM against alternate conditional methods, analyze its training stability, and visualize the learned flow paths. Subsequently, we model the dynamics of materials' microstructures undergoing spinodal decomposition across varied processing conditions. In this target

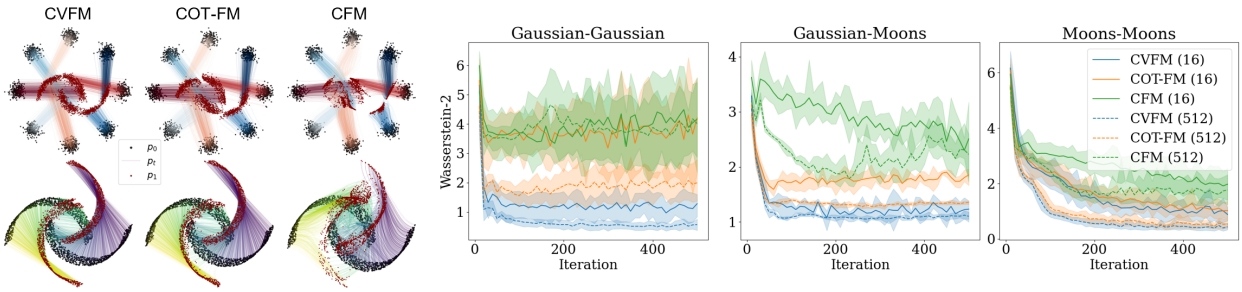

Figure 3. CVFM results in lower error in Wasserstein-2 distance to target distribution across batch sizes and conditional cost weighting η, compared to COT-FM (Eq. (10)) and the naïve conditional implementation CFM. Trajectories are colored by conditioning variable.

application, we test the cumulative performance in mapping between a series of conditional distributions with continuous conditioning. A third case study applying CVFM to high-dimensional domain transfer is left to Appendix D.5. Appendix D includes additional details regarding motivation and problem construction and Appendix E for further analysis.

2D Experiments: We evaluate our method on three 2D toy problems. Two problems with 8 discrete conditions – *8 Gaussians-Moons* testing large bifurcations and *8 Gaussians-8 Gaussians* testing strong conditional dependence – are used for comparison against prior methods. A third problem, *Moons-Moons*, involves continuous conditioning (Figure E.1). CVFM is benchmarked against Conditional Generative Flow Matching (CGFM) (Isobe et al., 2024; Zheng et al., 2023; Dao et al., 2023), Triangular Conditional Optimal Transport (T-COT-FM) (Kerrigan et al., 2024; Chemseddine et al., 2024), as well as two ablated CVFM variants. CGFM in particular does not support *unpaired* conditioning, requiring the ability to sample from $z \sim \{\pi(x_0, x_1|y_i)\}_{i=0}^m$, precluding its ability to address scientific questions as $m \to \infty$. We simply present it as a useful benchmark, representing a lower-bound in cases with discrete conditioning. The first ablated variant removes both mini-batch conditional OT and $\alpha(w)$, but retains the interpolated flow $p_t(y|w)$. We refer to this variant as Conditional Flow Matching (CFM) as it reduces to the original proposed CFM algorithm given paired samples (Lipman et al., 2023; Albergo & Vanden-Eijnden, 2023). The second variant solely excludes $\alpha(w)$ – we refer to this as Conditional Optimal Transport Flow Matching (COT-FM) – nearly equivalent to T-COT-FM; it differs by having varied noise schedules for the conditional probability paths $p_t(x|z)$ and $p_t(y|w)$. ODE and SDE-based variants for the SB problem are also evaluated for CVFM and COT-FM, utilizing the probability flow ODE with entropic regularized OT, alongside the SDE extension to our objective, conditional variable score and flow matching (CVSFM).

Three mappings are investigated and their associated results are displayed in Table 1, with the Wasserstein-2 error from the predicted distribution at $t = 1$ to the target distribution reported. The CVFM method notably results in equivalent or more optimal values of Wasserstein-2 error across all mappings with unpaired conditioning, nearly matching CGFM's performance on discrete problems where CGFM has knowledge of the correct conditional couplings *a priori*. Figure 3 contrasts samples and pathways from a subset of these methods. Notably, the kernel appreciably improves performance; CVFM outperforms both T-COT-FM and COT-FM, while the CFM formulation highlights the importance of the sampling from the conditional identity coupling: its absence precludes the validity of Eq. (7) (Appendix A) resulting in poor performance.

Improved convergence: CVFM also displays improved convergence characteristics, as evidenced by Figure 3. In all cases, the CVFM objective converges faster and to a lower metric value than other methods and variants. Further interrogation regarding the impact of η in the conditional ground cost and $\alpha(w)$ was also performed. In the proposed methods incorporating the ground cost (CVFM, COT-FM, and T-COT-FM), increasing η leads to improvement. However, it is often insufficient. For example, in the *8 Gaussian - 8 Gaussian* example the addition of $\alpha(w)$ in CVFM facilitates a marked improvement. Additional ablations

Table 1. Comparison of Wasserstein-2 error across conditional neural optimal transport and Schrödinger bridge methods, computed between the target distribution and simulated distribution at $t = 1$. Training was repeated over 5 seeds, with values reported as $\mu \pm \sigma$. Best observed values with *unpaired samples* are bolded with second best denoted by an asterisk within OT and SB methods. *Entropic* OT couplings identified via the Sinkhorn algorithm are differentiated from default *Exact* couplings, Eq. (3).

	Wasserstein-2 Error (↓)		
	8 Gaussian-Moons	8 Gaussian-8 Gaussian	Moons-Moons
CVFM	**0.440±0.097**	**0.571±0.139**	**1.102±0.047**
COT-FM	0.537±0.115*	1.997±0.528*	1.353±0.022
CFM	1.768±0.448	4.013±1.026	2.227±0.264
T-COT-FM	0.564±0.031	2.296±0.060	1.318±0.041*
CVFM-Entropic	**0.414±0.109**	**0.409±0.080**	**1.018±0.031**
COT-FM-Entropic	0.720±0.176	2.566±0.624	1.080±0.016*
CVSFM	0.428±0.114*	0.518±0.105*	1.081±0.028
COT-SFM	0.539±0.133	1.936±0.423	1.267±0.043
CGFM	0.352±0.085	0.491±0.095	–
CGFM-Entropic	0.376±0.083	0.483±0.075	–

are also presented in Appendix E.1 highlighting the important role of $\alpha(w)$ in reducing the error in the mini-batch COT approximation inherent in Eq. (10) in greater depth.

Material Dynamics: We next investigate the performance of our proposed method in a target scientific application: the dynamics of time-evolving microstructures subject to various processing conditions. Phase-field simulations are commonly applied to model a number of manufacturing processes involving evolving interfaces (e.g., solidification/melting, spinodal decomposition, grain growth, recrystallization, and crack propagation (Steinbach, 2009; Miehe et al., 2010)). These simulations are stochastic – the result of numerical noise representing thermal fluctuations, such that, even provided equivalent initial processing conditions, the resulting microstructure state over time will vary. In this experiment, we particularly focus on spinodal decomposition, applicable for material systems which undergo a thermodynamic phase transition resulting in the separation of a homogeneous mixture into distinct phases. The resulting dataset contains 100 simulation trajectories evaluated across 100 time steps – in total, 10,000 two-phase microstructures of dimension 256×256 voxels. Quantification of the internal state of each microstructure was performed by computing its 2-point spatial correlations (Kröner, 1971; Torquato, 2002), a representation quantifying material constituent internal spatial correlations, while also accounting for underlying symmetries (e.g., translation-equivariance and periodicity). Further discussion regarding this quantification procedure is presented in Appendix C. Individual correlations were then compressed to a 5-dimensional vector via Principal Component Analysis (PCA). In this problem, we use CVFM to model conditional time-dependent microstructural evolution, provided 100 sequential conditional empirical distributions.

Importantly, the time-dependent observations modeled are the result of computational simulations rather than high-cost intermittent experimental sampling, granting us complete access to *paired* conditioning-trajectory information – information frequently inaccessible in settings of interest. This enables us to validate and quantify the model's performance by computing error metrics on a per trajectory basis. Despite this, we still implement CVFM using *unpaired* data to mirror the experimental setting. Table 2 contrasts the trajectory absolute error of various potential surrogates for the dynamics. We evaluate CVSFM – the SDE extension to CVFM – and alternate neural OT methods – using *unpaired* samples and conditioning variables – against traditional approaches (Neural ODEs and LSTMs) requiring complete trajectory information. To ensure fair comparison, Neural ODE and LSTM baselines were tuned to have approximately equivalent parameter counts to CVFM; see Appendix D.6 for details. Despite only having access to corrupted and *misaligned* versions of the available observations, CVSFM-Exact results in lower mean absolute errors across

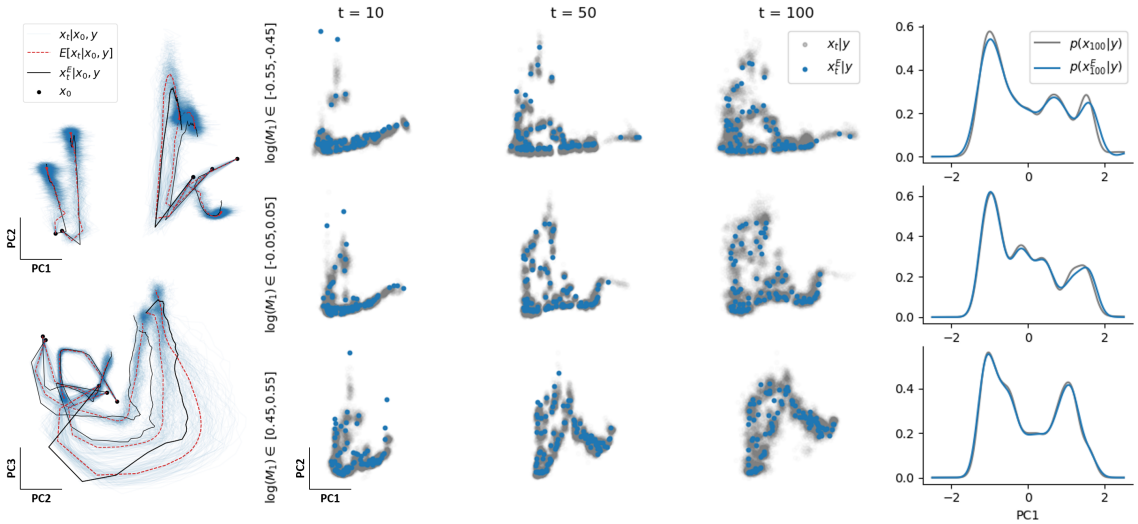

Figure 4. Collection of 5 randomly sampled trajectories from the test set in projections of PC1-PC2 and PC2-PC3 displaying (left) samples in blue from CVSFM-Exact, with the expected value as a function of time in red. Comparison of test marginal densities (middle) constructed as narrow subsets of first constituent's mobility ($\mathcal{M}_1$) parameter, in PC1-PC2 projection, and (right) marginal comparison of final state at $t = 100$ for PC1. 128 samples were simulated for each (x_0, y).

Table 2. Comparison of conditional neural optimal transport methods alongside conventional approaches on spinodal decomposition PC trajectories. Reported mean absolute errors are computed between predicted trajectories and target trajectories not observed during training across all times. Expected values, $\mathbb{E}[x_t|x_0, y]$, are used for stochastic predictions. Reported absolute error metrics are reported as $\mu \pm \sigma$ alongside maximum and minimum values.

	Train			Test		
	$\mu \pm \sigma$	Min.	Max.	$\mu \pm \sigma$	Min.	Max.
Neural ODE	0.261±0.119	0.105	**1.499**	0.264±0.129	0.116	1.400
LSTM	0.355±0.212	0.038	2.071	0.358±0.331	0.045	1.648
CVSFM	**0.166±0.140**	**0.023**	1.654	**0.188±0.147**	0.039	**1.284**
CVSFM-Entropic	0.378±0.322	0.045	2.112	0.388±0.320	0.044	2.032
COT-SFM	0.202±0.348	0.034	11.422	0.218±0.489	**0.033**	11.649
COT-SFM-Entropic	0.524±0.306	0.108	2.568	0.531±0.307	0.110	2.012
T-COT-FM	0.899±0.370	0.163	3.47	0.901±0.365	0.161	2.639
T-COT-SFM	0.636±0.279	0.235	2.331	0.637±0.282	0.194	2.335

expected trajectories. CVSFM-Exact also outperforms alternatives such as T-COT-FM (Kerrigan et al., 2024) and an SDE-based extension, denoted as T-COT-SFM.

The superior performance of CVSFM over paired baselines can be attributed to the specific nature of spinodal decomposition dynamics. The Cahn-Hilliard equation exhibits stiff dynamics, characterized by rapid high-gradient phase separation in early time steps followed by slower coarsening. The deterministic baseline models (i.e., NeuralODE, LSTM) are highly sensitive to approximation errors in these early high-gradient regimes; slight deviations cause the trajectory to diverge from the data manifold, leading to compounding errors across subsequent time points. In contrast, the SDE formulation of CVSFM incorporates a learned score function, $\nabla \log p(x|y)$, which acts as a restorative field. During sampling, this score term effectively guides the trajectory back towards high-density regions of the probability path, correcting for numerical

Table 3. Comparison of time-averaged Wasserstein-2 error between predicted marginal distributions and test data for binned mobility $\log(\mathcal{M}_1)$ values.

	Wasserstein-2 Error (↓)		
	$[-0.55, -0.45]$	$[-0.05, 0.05]$	$[0.45, 0.55]$
CVSFM	**0.637**	0.628	**0.646**
CVSFM-Entropic	0.886	1.213	1.523
COT-SFM	0.674	**0.608**	0.690
COT-SFM-Entropic	1.129	1.329	1.997

drift caused by the stiff early dynamics and allowing CVSFM to maintain physical fidelity over longer time horizons.

We next examine CVFM's ability to accurately learn the stochasticity in the process dynamics of the microstructure in a distributional sense. Because the conditioning variables are continuous, we only have one unique trajectory $\{(x_i, y_i)\}_{i=0}^{T=99}$ for each given y. To overcome this limitation, we defined three narrow subsets based on the first mobility parameter $\mathcal{M}_1$, covering the test dataset. The remaining parameters $(\mathcal{M}_2, c_0)$ are not constrained. Table 3 presents the time-averaged Wasserstein-2 errors across all observed marginals for variants of CVSFM and COT-SFM on these subsets. CVSFM accurately reconstructs the marginal distributions. Figure 4 displays sample trajectories, along with the evolving time distributions for these subsets, and their corresponding marginalized density estimates along the first principal component for CVSFM. The network captures the change in the width and shape of the distribution over time. Overall, the performance on individual trajectories and observed marginals highlights the proposed method's effectiveness in capturing complex conditional stochastic nonlinear dynamics.

5 Conclusion

We have proposed Conditional Variable Flow Matching (CVFM), a novel framework capable of learning to transform conditional distributions between general source and target distributions given *unpaired* samples. Building on this foundation, we also present extensions capable of approximating the conditional Schrödinger bridge problem. Our central contribution is a rigorous algorithmic framework equipped with a regularized conditional distance metric, an independent conditioning variable flow, and a conditioning mismatch kernel that enforces *local consistency* across the learned vector fields. We verify our approach through synthetic and real-world tasks, demonstrating a robust, simulation-free framework for learning conditional stochastic dynamical processes even in regimes where standard methods suffer from deleterious instabilities.

References

Brent L. Adams, Surya R. Kalidindi, and David T. Fullwood. Microstructure-Sensitive Design for Performance Optimization. In *Microstructure Sensitive Design for Performance Optimization*, pp. i. Elsevier, 2013. ISBN 978-0-12-396989-7. doi: 10.1016/B978-0-12-396989-7.01001-7. URL https://linkinghub.elsevier.com/retrieve/pii/B9780123969897010017.

Michael S. Albergo and Eric Vanden-Eijnden. Building Normalizing Flows with Stochastic Interpolants, March 2023. URL http://arxiv.org/abs/2209.15571. arXiv:2209.15571 [cs, stat].

Michael S. Albergo, Nicholas M. Boffi, and Eric Vanden-Eijnden. Stochastic Interpolants: A Unifying Framework for Flows and Diffusions, March 2023. URL http://arxiv.org/abs/2303.08797. arXiv:2303.08797 [cond-mat].

ASTM International. Standard Test Methods and Definitions for Mechanical Testing of Steel Products, March 2024. URL https://compass.astm.org/document/?contentCode=ASTM%7CA0370-24%7Cen-US&proxycl=https%3A%2F%2Fsecure.astm.org&fromLogin=true.

Ricardo Baptista, Aram-Alexandre Pooladian, Michael Brennan, Youssef Marzouk, and Jonathan Niles-Weed. Conditional simulation via entropic optimal transport: Toward non-parametric estimation of conditional Brenier maps, November 2024. URL http://arxiv.org/abs/2411.07154. arXiv:2411.07154 [stat].

Charlotte Bunne, Andreas Krause, and Marco Cuturi. Supervised Training of Conditional Monge Maps. *Advances in Neural Information Processing Systems*, 35:6859–6872, December 2022. URL https://proceedings.neurips.cc/paper_files/paper/2022/hash/2d880acd7b31e25d45097455c8e8257f-Abstract-Conference.html.

Charlotte Bunne, Ya-Ping Hsieh, Marco Cuturi, and Andreas Krause. The Schr\"odinger Bridge between Gaussian Measures has a Closed Form, March 2023a. URL http://arxiv.org/abs/2202.05722. arXiv:2202.05722 [cs, q-bio].

Charlotte Bunne, Stefan G. Stark, Gabriele Gut, Jacobo Sarabia del Castillo, Mitch Levesque, Kjong-Van Lehmann, Lucas Pelkmans, Andreas Krause, and Gunnar Rätsch. Learning single-cell perturbation responses using neural optimal transport. *Nature Methods*, 20(11):1759–1768, November 2023b. ISSN 1548-7105. doi: 10.1038/s41592-023-01969-x. URL https://www.nature.com/articles/s41592-023-01969-x. Publisher: Nature Publishing Group.

John W. Cahn and John E. Hilliard. Free Energy of a Nonuniform System. I. Interfacial Free Energy. *Journal of Chemical Physics*, 28:258–267, February 1958. ISSN 0021-96060301-0104. doi: 10.1063/1.1744102. URL https://ui.adsabs.harvard.edu/abs/1958JChPh..28..258C. ADS Bibcode: 1958JChPh..28..258C.

Jannis Chemseddine, Paul Hagemann, Gabriele Steidl, and Christian Wald. Conditional Wasserstein Distances with Applications in Bayesian OT Flow Matching, June 2024. URL http://arxiv.org/abs/2403.18705. arXiv:2403.18705 [cs, math].

Ricky T. Q. Chen, Yulia Rubanova, Jesse Bettencourt, and David K Duvenaud. Neural Ordinary Differential Equations. In *Advances in Neural Information Processing Systems*, volume 31. Curran Associates, Inc., 2018. URL https://proceedings.neurips.cc/paper_files/paper/2018/hash/69386f6bb1dfed68692a24c8686939b9-Abstract.html.

Tianrong Chen, Guan-Horng Liu, and Evangelos A. Theodorou. Likelihood Training of Schr\"odinger Bridge using Forward-Backward SDEs Theory, April 2023. URL http://arxiv.org/abs/2110.11291. arXiv:2110.11291 [cs, math, stat].

Yihui Chen, Yanfei Chen, Dawei Wang, and Shigang Ai. Generating 3D digital material twins for woven ceramic-matrix composites from uCT images. *Journal of the American Ceramic Society*, 105(1):481–497, 2022. ISSN 1551-2916. doi: 10.1111/jace.18044. URL https://onlinelibrary.wiley.com/doi/abs/10.1111/jace.18044.

Yongxin Chen, Tryphon T. Georgiou, and Michele Pavon. Optimal Transport in Systems and Control. *Annual Review of Control, Robotics, and Autonomous Systems*, 4(Volume 4, 2021):89–113, May 2021. ISSN 2573-5144. doi: 10.1146/annurev-control-070220-100858. URL https://www.annualreviews.org/content/journals/10.1146/annurev-control-070220-100858. Publisher: Annual Reviews.

Marco Cuturi. Sinkhorn Distances: Lightspeed Computation of Optimal Transport. In *Advances in Neural Information Processing Systems*, volume 26. Curran Associates, Inc., 2013. URL https://papers.nips.cc/paper_files/paper/2013/hash/af21d0c97db2e27e13572cbf59eb343d-Abstract.html.

Quan Dao, Hao Phung, Binh Nguyen, and Anh Tran. Flow Matching in Latent Space, July 2023. URL http://arxiv.org/abs/2307.08698. arXiv:2307.08698 [cs].

Valentin De Bortoli, James Thornton, Jeremy Heng, and Arnaud Doucet. Diffusion Schrödinger Bridge with Applications to Score-Based Generative Modeling. In *Advances in Neural Information Processing Systems*, volume 34, pp. 17695–17709. Curran Associates, Inc., 2021. URL https://proceedings.neurips.cc/paper_files/paper/2021/hash/940392f5f32a7ade1cc201767cf83e31-Abstract.html.

Valentin De Bortoli, James Thornton, Jeremy Heng, and Arnaud Doucet. Diffusion Schr\"odinger Bridge with Applications to Score-Based Generative Modeling, April 2023. URL http://arxiv.org/abs/2106.01357. arXiv:2106.01357 [cs, math, stat].

R Dingreville, J A Stewart, and E Y Chen. Benchmark problems for the Mesoscale Multiphysics Phase Field Simulator (MEMPHIS). Technical report, April 2020.

Kilian Fatras, Younes Zine, Rémi Flamary, Rémi Gribonval, and Nicolas Courty. Learning with minibatch Wasserstein : asymptotic and gradient properties, October 2021a. URL http://arxiv.org/abs/1910.04091. arXiv:1910.04091 [cs, stat].

Kilian Fatras, Younes Zine, Szymon Majewski, Rémi Flamary, Rémi Gribonval, and Nicolas Courty. Minibatch optimal transport distances; analysis and applications, January 2021b. URL http://arxiv.org/abs/2101.01792. arXiv:2101.01792 [cs, stat].

Mike Fisher, Jorge Nocedal, Yannick Trémolet, and Stephen J. Wright. Data assimilation in weather forecasting: a case study in PDE-constrained optimization. *Optimization and Engineering*, 10(3): 409–426, September 2009. ISSN 1389-4420, 1573-2924. doi: 10.1007/s11081-008-9051-5. URL http://link.springer.com/10.1007/s11081-008-9051-5.

Rémi Flamary, Nicolas Courty, Alexandre Gramfort, Mokhtar Z. Alaya, Aurélie Boisbunon, Stanislas Chambon, Laetitia Chapel, Adrien Corenflos, Kilian Fatras, Nemo Fournier, Léo Gautheron, Nathalie T. H. Gayraud, Hicham Janati, Alain Rakotomamonjy, Ievgen Redko, Antoine Rolet, Antony Schutz, Vivien Seguy, Danica J. Sutherland, Romain Tavenard, Alexander Tong, and Titouan Vayer. POT: Python Optimal Transport. *Journal of Machine Learning Research*, 22(78):1–8, 2021. ISSN 1533-7928. URL http://jmlr.org/papers/v22/20-451.html.

Adam P. Generale and Surya R. Kalidindi. Reduced-order models for microstructure-sensitive effective thermal conductivity of woven ceramic matrix composites with residual porosity. *Composite Structures*, 274:114399, October 2021. ISSN 02638223. doi: 10.1016/j.compstruct.2021.114399. URL https://linkinghub.elsevier.com/retrieve/pii/S0263822321008618.

Reza Ghanavati and Homam Naffakh-Moosavy. Additive manufacturing of functionally graded metallic materials: A review of experimental and numerical studies. *Journal of Materials Research and Technology*, 13:1628–1664, July 2021. ISSN 2238-7854. doi: 10.1016/j.jmrt.2021.05.022. URL https://www.sciencedirect.com/science/article/pii/S2238785421004622.

Akash Gupta, Ahmet Cecen, Sharad Goyal, Amarendra K. Singh, and Surya R. Kalidindi. Structure–property linkages using a data science approach: Application to a non-metallic inclusion/steel

composite system. *Acta Materialia*, 91:239–254, June 2015. ISSN 1359-6454. doi: 10.1016/j.actamat.2015.02.045. URL http://www.sciencedirect.com/science/article/pii/S1359645415001603.

Grayson H. Harrington, Conlain Kelly, Vahid Attari, Raymundo Arroyave, and Surya R. Kalidindi. Application of a Chained-ANN for Learning the Process-Structure Mapping in Mg2SixSn1-x Spinodal Decomposition. *Integrating Materials and Manufacturing Innovation*, 11(3):433–449, September 2022. ISSN 2193-9772. doi: 10.1007/s40192-022-00274-3. URL https://doi.org/10.1007/s40192-022-00274-3.

Benedek Harsanyi, Marianna Rapsomaniki, and Jannis Born. Learning Drug Perturbations via Conditional Map Estimators. March 2024. URL https://openreview.net/forum?id=FE7lRuwmfI.

Dan Hendrycks and Kevin Gimpel. Gaussian Error Linear Units (GELUs), June 2023. URL http://arxiv.org/abs/1606.08415. arXiv:1606.08415 [cs].

Jonathan Ho and Tim Salimans. Classifier-Free Diffusion Guidance, July 2022. URL http://arxiv.org/abs/2207.12598. arXiv:2207.12598 [cs].

Jonathan Ho, Ajay Jain, and Pieter Abbeel. Denoising Diffusion Probabilistic Models, December 2020. URL http://arxiv.org/abs/2006.11239. arXiv:2006.11239 [cs, stat].

Sepp Hochreiter and Jürgen Schmidhuber. Long Short-Term Memory. *Neural Computation*, 9(8):1735–1780, November 1997. ISSN 0899-7667. doi: 10.1162/neco.1997.9.8.1735. URL https://ieeexplore.ieee.org/abstract/document/6795963. Conference Name: Neural Computation.

Noboru Isobe, Masanori Koyama, Kohei Hayashi, and Kenji Fukumizu. Extended Flow Matching: a Method of Conditional Generation with Generalized Continuity Equation, March 2024. URL http://arxiv.org/abs/2402.18839. arXiv:2402.18839 [cs, math].

Surya R. Kalidindi. *Hierarchical Materials Informatics: Novel Analytics for Materials Data*. Butterworth-Heinemann, Amsterdam, 1st edition edition, August 2015. ISBN 978-0-12-410394-8.

Surya R. Kalidindi. Feature engineering of material structure for AI-based materials knowledge systems. *Journal of Applied Physics*, 128(4):041103, July 2020. ISSN 0021-8979. doi: 10.1063/5.0011258. URL https://aip.scitation.org/doi/10.1063/5.0011258. Publisher: American Institute of Physics.

Tero Karras, Miika Aittala, Timo Aila, and Samuli Laine. Elucidating the Design Space of Diffusion-Based Generative Models, October 2022. URL http://arxiv.org/abs/2206.00364. arXiv:2206.00364 [cs, stat].

Gavin Kerrigan, Giosue Migliorini, and Padhraic Smyth. Dynamic Conditional Optimal Transport through Simulation-Free Flows, May 2024. URL http://arxiv.org/abs/2404.04240. arXiv:2404.04240.

Ekkehart Kröner. *Statistical Continuum Mechanics*, volume 92 of *CISM International Centre for Mechanical Sciences*. Springer Vienna, Vienna, 1971. ISBN 978-3-211-81129-0. doi: 10.1007/978-3-7091-2862-6. URL http://link.springer.com/10.1007/978-3-7091-2862-6.

Marat I. Latypov, Laszlo S. Toth, and Surya R. Kalidindi. Materials knowledge system for nonlinear composites. *Computer Methods in Applied Mechanics and Engineering*, 346:180–196, April 2019. ISSN 0045-7825. doi: 10.1016/j.cma.2018.11.034. URL http://www.sciencedirect.com/science/article/pii/S0045782518305930.

Yaron Lipman, Ricky T Q Chen, Heli Ben-Hamu, Maximilian Nickel, and Matt Le. Flow Matching for Generative Modeling. 2023.

Guan-Horng Liu, Tianrong Chen, Oswin So, and Evangelos Theodorou. Deep Generalized Schrödinger Bridge. *Advances in Neural Information Processing Systems*, 35:9374–9388, December 2022a. URL https://proceedings.neurips.cc/paper_files/paper/2022/hash/3d17b7f7d52c83ab6e97e2dc0bda2e71-Abstract-Conference.html.

Xingchao Liu, Chengyue Gong, and Qiang Liu. Flow Straight and Fast: Learning to Generate and Transfer Data with Rectified Flow, September 2022b. URL http://arxiv.org/abs/2209.03003. arXiv:2209.03003 [cs].

Zhiyuan Liu, Dandan Zhao, Pei Wang, Ming Yan, Can Yang, Zhangwei Chen, Jian Lu, and Zhaoping Lu. Additive manufacturing of metals: Microstructure evolution and multistage control. *Journal of Materials Science & Technology*, 100:224–236, February 2022c. ISSN 1005-0302. doi: 10.1016/j.jmst.2021.06.011. URL https://www.sciencedirect.com/science/article/pii/S1005030221006046.

Turab Lookman, Prasanna V. Balachandran, Dezhen Xue, and Ruihao Yuan. Active learning in materials science with emphasis on adaptive sampling using uncertainties for targeted design. *npj Computational Materials*, 5(1):1–17, February 2019. ISSN 2057-3960. doi: 10.1038/s41524-019-0153-8. URL https://www.nature.com/articles/s41524-019-0153-8. Publisher: Nature Publishing Group.

Ilya Loshchilov and Frank Hutter. Decoupled Weight Decay Regularization, January 2019. URL http://arxiv.org/abs/1711.05101. arXiv:1711.05101 [cs, math].

Christian Léonard. From the Schr\"odinger problem to the Monge-Kantorovich problem, November 2010. URL https://arxiv.org/abs/1011.2564v1.

Christian Léonard. A survey of the Schr\"odinger problem and some of its connections with optimal transport, August 2013. URL http://arxiv.org/abs/1308.0215. arXiv:1308.0215 [math].

Andrew Marshall and Surya R. Kalidindi. Autonomous Development of a Machine-Learning Model for the Plastic Response of Two-Phase Composites from Micromechanical Finite Element Models. *JOM*, 73(7): 2085–2095, July 2021. ISSN 1543-1851. doi: 10.1007/s11837-021-04696-w. URL https://doi.org/10.1007/s11837-021-04696-w.

Christian Miehe, Martina Hofacker, and Fabian Welschinger. A phase field model for rate-independent crack propagation: Robust algorithmic implementation based on operator splits. *Computer Methods in Applied Mechanics and Engineering*, 199(45):2765–2778, November 2010. ISSN 0045-7825. doi: 10.1016/j.cma.2010.04.011. URL https://www.sciencedirect.com/science/article/pii/S0045782510001283.

Toshio Mikami. Monge's problem with a quadratic cost by the zero-noise limit of h-path processes. *Probability Theory and Related Fields*, 129(2):245–260, June 2004. ISSN 1432-2064. doi: 10.1007/s00440-004-0340-4. URL https://doi.org/10.1007/s00440-004-0340-4.

Toshio Mikami and Michèle Thieullen. Duality theorem for the stochastic optimal control problem. *Stochastic Processes and their Applications*, 116(12):1815–1835, December 2006. ISSN 0304-4149. doi: 10.1016/j.spa.2006.04.014. URL https://www.sciencedirect.com/science/article/pii/S0304414906000627.

David Montes de Oca Zapiain, James A. Stewart, and Rémi Dingreville. Accelerating phase-field-based microstructure evolution predictions via surrogate models trained by machine learning methods. *npj Computational Materials*, 7(1):1–11, January 2021. ISSN 2057-3960. doi: 10.1038/s41524-020-00471-8. URL https://www.nature.com/articles/s41524-020-00471-8. Number: 1 Publisher: Nature Publishing Group.

Stephen R. Niezgoda, Yuksel C. Yabansu, and Surya R. Kalidindi. Understanding and visualizing microstructure and microstructure variance as a stochastic process. *Acta Materialia*, 59(16):6387–6400, September 2011. ISSN 1359-6454. doi: 10.1016/j.actamat.2011.06.051. URL https://www.sciencedirect.com/science/article/pii/S1359645411004654.

Noah H. Paulson, Matthew W. Priddy, David L. McDowell, and Surya R. Kalidindi. Reduced-order structure-property linkages for polycrystalline microstructures based on 2-point statistics. *Acta Materialia*, 129: 428–438, May 2017. ISSN 1359-6454. doi: 10.1016/j.actamat.2017.03.009. URL http://www.sciencedirect.com/science/article/pii/S135964541730188X.

Gabriel Peyré and Marco Cuturi. Computational Optimal Transport, March 2020. URL http://arxiv.org/abs/1803.00567. arXiv:1803.00567 [stat].

Aram-Alexandre Pooladian, Heli Ben-Hamu, Carles Domingo-Enrich, Brandon Amos, Yaron Lipman, and Ricky T. Q. Chen. Multisample Flow Matching: Straightening Flows with Minibatch Couplings, May 2023. URL http://arxiv.org/abs/2304.14772. arXiv:2304.14772 [cs].

Domènec Ruiz-Balet and Enrique Zuazua. Neural ODE Control for Classification, Approximation, and Transport. *SIAM Review*, 65(3):735–773, August 2023. ISSN 0036-1445. doi: 10.1137/21M1411433. URL https://epubs.siam.org/doi/abs/10.1137/21M1411433. Publisher: Society for Industrial and Applied Mathematics.

George F. Schrader and Ahmad K. Elshennawy. *Manufacturing Processes and Materials, Fourth Edition*. Society of Manufacturing Engineers, 2000. ISBN 978-0-87263-517-3. Google-Books-ID: Nz2wXvmkAF0C.

E. Schrödinger. Sur la théorie relativiste de l'électron et l'interprétation de la mécanique quantique. *Annales de l'institut Henri Poincaré*, 2(4):269–310, 1932. ISSN 2400-4855. URL http://www.numdam.org/item/AIHP_1932__2_4_269_0/.

Yuyang Shi, Valentin De Bortoli, Andrew Campbell, and Arnaud Doucet. Diffusion Schr\"odinger Bridge Matching, December 2023. URL http://arxiv.org/abs/2303.16852. arXiv:2303.16852 [cs, stat].

Yang Song, Jascha Sohl-Dickstein, Diederik P Kingma, Abhishek Kumar, Stefano Ermon, and Ben Poole. Score-based Generative Modeling Through Stochastic Differential Equations. 2021.

Ingo Steinbach. Phase-field models in materials science. *Modelling and Simulation in Materials Science and Engineering*, 17(7):073001, July 2009. ISSN 0965-0393. doi: 10.1088/0965-0393/17/7/073001. URL https://dx.doi.org/10.1088/0965-0393/17/7/073001.

Esteban G. Tabak, Giulio Trigila, and Wenjun Zhao. Data Driven Conditional Optimal Transport, October 2019. URL http://arxiv.org/abs/1910.11422. arXiv:1910.11422 [math].

Zhicong Tang, Tiankai Hang, Shuyang Gu, Dong Chen, and Baining Guo. Simplified Diffusion Schr\"odinger Bridge, March 2024. URL http://arxiv.org/abs/2403.14623. arXiv:2403.14623 [cs].

Alexander Tong, Nikolay Malkin, Kilian Fatras, Lazar Atanackovic, Yanlei Zhang, Guillaume Huguet, Guy Wolf, and Yoshua Bengio. Simulation-free Schr\"odinger bridges via score and flow matching, October 2023a. URL http://arxiv.org/abs/2307.03672. arXiv:2307.03672 [cs].

Alexander Tong, Nikolay Malkin, Guillaume Huguet, Yanlei Zhang, Jarrid Rector-Brooks, Kilian Fatras, Guy Wolf, and Yoshua Bengio. Improving and Generalizing Flow-Based Generative Models with Minibatch Optimal Transport. July 2023b. URL https://openreview.net/forum?id=HgDwiZrpVq.

Salvatore Torquato. *Random Heterogeneous Materials: Microstructure and Macroscopic Properties*. Interdisciplinary Applied Mathematics. Springer-Verlag, New York, 2002. ISBN 978-0-387-95167-6. doi: 10.1007/978-1-4757-6355-3. URL https://www.springer.com/gp/book/9780387951676.

Anh Tran, John A. Mitchell, Laura P. Swiler, and Tim Wildey. An active learning high-throughput microstructure calibration framework for solving inverse structure–process problems in materials informatics. *Acta Materialia*, 194:80–92, August 2020. ISSN 1359-6454. doi: 10.1016/j.actamat.2020.04.054. URL https://www.sciencedirect.com/science/article/pii/S1359645420303220.

Francisco Vargas. Machine-learning approaches for the empirical Schrödinger bridge problem. Technical Report 958, University of Cambridge, June 2021.

Cédric Villani. *Optimal Transport*, volume 338 of *Grundlehren der mathematischen Wissenschaften*. Springer, Berlin, Heidelberg, 2009. ISBN 978-3-540-71049-3. doi: 10.1007/978-3-540-71050-9. URL http://link.springer.com/10.1007/978-3-540-71050-9.

Yuksel C. Yabansu, Patrick Altschuh, Johannes Hötzer, Michael Selzer, Britta Nestler, and Surya R. Kalidindi. A digital workflow for learning the reduced-order structure-property linkages for permeability of porous membranes. *Acta Materialia*, 195:668–680, August 2020. ISSN 1359-6454. doi: 10.1016/j.actamat.2020.06.003. URL http://www.sciencedirect.com/science/article/pii/S1359645420304274.

Qinqing Zheng, Matt Le, Neta Shaul, Yaron Lipman, Aditya Grover, and Ricky T. Q. Chen. Guided Flows for Generative Modeling and Decision Making, December 2023. URL http://arxiv.org/abs/2311.13443. arXiv:2311.13443 [cs, stat].

A Appendix: Proofs of Theorems

A.1 Proof $p_t(x|y)$ and $u_t(x|y)$ satisfy the continuity equation

Theorem 3.1 *The marginal conditional vector field Eq. (7) generates the marginal conditional probability path Eq. (6) from $p_0(x|y)$ given samples of $q(z,w)$ if $q(y_0) = q(y_1)$ and (x_0, y_0) and (x_1, y_1) are drawn from $q(z,w)$ following the conditional optimal coupling $\pi(y_0, y_1)$ over w.*

Proof. The continuity equation provides a necessary and sufficient condition for a vector field to generate a probability distribution (Villani, 2009). Therefore, the proof is completed by demonstrating that $u_t(x|y)$, defined by Eq. (7), meets the continuity equation for the conditional distribution $p_t(x|y)$. We utilize the assumed decomposition introduced in the main body of the paper, $p(x,y|z,w) = p(x|z)p(y|w)$. Additionally, we assume that x is independent of w given y, $p_t(x|y,w) = p_t(x|y)$. Finally, we will require that $p(y_0) = p(y_1)$. In other words, that the distribution on the conditioning variable is the same at t_0 and t_1. We argue that this is not a very restrictive requirement in practice. It is the situation that occurs in many applications, in particular scientific dynamics problems where the distribution on conditions is constant over all time.

$$\frac{d}{dt}\left(p_t(x|y)\right) = -\mathrm{div}_x(p_t(x|y)u_t(x|y)) \tag{A.1}$$

We begin with expanding the left hand side of the continuity equation in Eq. (A.1). To clarify notation, we utilize $p(\cdot)$ to denote probability density functions over the primary variables, x and y. We use $q(\cdot)$ to denote distributions over the pair variables z and w. The subscript t denotes time dependence. Their arguments differentiate the multiple distributions of each type.

$$\begin{aligned}\frac{d}{dt}\left(p_t(x|y)\right) &= \frac{d}{dt}\left(\frac{p_t(x,y)}{p_t(y)}\right)\\ &= \frac{d}{dt}\left(\int \frac{p_t(x,y|w,z)}{p_t(y)} q(w,z)dzdw\right)\end{aligned}$$

We utilize the following assumed decomposition, $p_t(x,y|w,z) = p_t(x|z)p_t(y|w)$,

$$\begin{aligned}&= \frac{d}{dt}\left(\int \frac{p_t(x|z)p_t(y|w)}{p_t(y)} q(w,z)dzdw\right)\\ &= \int \left[\underbrace{\frac{p_t(y|w)}{p_t(y)}\frac{d}{dt}(p_t(x|z))}_{T_1} - \underbrace{\frac{p_t(x|z)p_t(y|w)}{p_t(y)^2}\frac{d}{dt}(p_t(y))}_{T_2} + \underbrace{\frac{p_t(x|z)}{p_t(y)}\frac{d}{dt}(p_t(y|w))}_{T_3}\right] q(w,z)dzdw\end{aligned}$$

We next consider each of the individual terms above. We will extensively rely upon the fact that we have prescribed forms to $u_t(x|z)$ and $u_t(y|w)$ such that they generate $p_t(x|z)$ and $p_t(y|w)$, respectively (see Theorem 3 of Lipman et al. (2023) or Theorem 2.1 in Tong et al. (2023b)). The integrands are further assumed to satisfy the regularity conditions of the Leibniz Rule for changing the order of integration and differentiation. Beginning with the first term, T_1,

$$T_1 = \int \frac{p_t(y|w)}{p_t(y)}\frac{d}{dt}(p_t(x|z))q(w,z)dzdw$$

as $u(x|z)$ generates $p(x|z)$,

$$= -\int \frac{p_t(y|w)}{p_t(y)} \text{div}_x(p_t(x|z)u_t(x|z))q(w,z)dzdw$$

Leibniz Rule,

$$= -\text{div}_x\left(\int \frac{p_t(y|w)p_t(x|z)q(w,z)}{p_t(y)} u_t(x|z)dzdw\right)$$
$$= -\text{div}_x\left(p_t(x|y)\int \frac{p_t(y|w)p_t(x|z)q(w,z)}{p_t(y)p_t(x|y)} u_t(x|z)dzdw\right)$$

using the definition of $u_t(x|y)$, Eq. (7),

$$= -\text{div}_x\left(p_t(x|y)u_t(x|y)\right)$$

Here, we arrive at the right hand side of the continuity equation. Next, we turn to demonstrating that terms T_2 and T_3 equate to zero. We begin inspecting the second term, T_2,

$$T_2 = \int -\frac{p_t(x|z)p_t(y|w)}{p_t(y)^2}\frac{d}{dt}(p_t(y))q(w,z)dzdw$$
$$= -\frac{1}{p_t(y)^2}\frac{d}{dt}(p_t(y))\int p_t(x|z)p_t(y|w)q(w,z)dzdw$$
$$= -\frac{p_t(x|y)}{p_t(y)}\frac{d}{dt}p_t(y)$$

Next, we consider the last term, T_3, before returning to T_2.

$$T_3 = \int \frac{p_t(x|z)}{p_t(y)}\frac{d}{dt}(p_t(y|w))q(w,z)dzdw$$

as $u_t(y|w)$ generates $p_t(y|w)$,

$$= -\int \frac{p_t(x|z)}{p_t(y)}\text{div}_y(p_t(y|w)u_t(y|w))q(w,z)dzdw$$

Leibniz Rule,

$$= -\frac{1}{p_t(y)}\text{div}_y\left(\int u_t(y|w)p_t(x|z)p_t(y|w)q(w,z)dzdw\right)$$

marginalization on z, the chain rule of probability, and the second assumption outlined previously,

$$= -\frac{1}{p_t(y)}\text{div}_y\left(\int u_t(y|w)p_t(x|y)p_t(y|w)q(w)dw\right)$$
$$= -\frac{1}{p_t(y)}\text{div}_y\left(p_t(x|y)p_t(y)\int u_t(y|w)\frac{p_t(y|w)q(w)}{p_t(y)}dw\right)$$

definition of the marginal vector field, Eq. (8) in Lipman et al. (2023) or Eq. (9) in Tong et al. (2023b)

$$= -\frac{1}{p_t(y)} \text{div}_y \left(p_t(x|y) p_t(y) u_t(y) \right)$$

product rule,

$$= -\frac{1}{p_t(y)} p_t(y) u_t(y)^T \nabla_y p_t(x|y) - \frac{p_t(x|y)}{p_t(y)} \text{div}_y \left(p_t(y) u_t(y) \right)$$

$u_t(y)$ generates $p_t(y)$,

$$\begin{aligned} &= -\frac{1}{p_t(y)} p_t(y) u_t(y)^T \nabla_y p_t(x|y) + \frac{p_t(x|y)}{p_t(y)} \frac{d}{dt} p_t(y) \\ &= -u_t(y)^T \nabla_y p_t(x|y) + \frac{p_t(x|y)}{p_t(y)} \frac{d}{dt} p_t(y) \end{aligned}$$

Combining T_1, T_2, and T_3 together, we obtain,

$$\begin{aligned} \frac{d}{dt} \left(p_t(x|y) \right) &= T_1 + T_2 + T_3 \\ &= -\text{div}_x \left(p_t(x|y) u_t(x|y) \right) - \frac{p_t(x|y)}{p_t(y)} \frac{d}{dt} p_t(y) - u_t(y)^T \nabla_y p_t(x|y) + \frac{p_t(x|y)}{p_t(y)} \frac{d}{dt} p_t(y) \\ &= -\text{div}_x \left(p_t(x|y) u_t(x|y) \right) - u_t(y)^T \nabla_y p_t(x|y) \end{aligned}$$

Optimal Transport between $q(y_0) = q(y_1)$: The continuity equation is left with $-u_t(y)^T \nabla_y p_t(x|y)$. In general, this remainder is nonzero. For arbitrary empirical distributions $q(x_0, y_0)$ and $q(x_1, y_1)$, the $u_t(x|y)$ defined by Eq. (7) generates $p_t(x|y)$ only if the flow over y is carefully designed, such that it is orthogonal to $\nabla_y p_t(x|y)$ for all t.

In fact, in the problem settings discussed in this paper and under the proposed CVFM training scheme, we are in one of these rare situations. Consider our final assumption: $q(y_0) = q(y_1)$. In other words, we assume that the underlying distributions – represented by the empirical set of observations – of the conditioning variables at the boundary times are equivalent. Importantly, the set of samples representing each distribution implicitly are not equal. Additionally, the set sizes can be imbalanced. When $q(y_0) = q(y_1)$, the optimal transport plan is the identity coupling. This results in zero displacement, and as such, the marginal velocity field $u_t(y) = 0$ for all $t \in [0, 1]$. Importantly, in CVFM, we only utilize a conditional flow, $u_t(y|w)$, which approximates the flow over y, $u_t(y)$, in expectation. In general, this type of conditional approximation is not guaranteed to produce the marginal optimal transport map. However, when static optimal transport is utilized in training, Tong et al. (2023a); Pooladian et al. (2023) show that this results in the expectation of the conditional flow sufficiently approximating the marginal OT.

In fact, we directly observed the impact of mini-batch OT (and the scaling kernel) and this remainder in the first presented case study. Without mini-batch OT, the learned $u_t(x|y)$ cannot generate the required marginal conditional vector field generating $p_t(x|y)$. Only once conditional optimal transport was incorporated could the appropriate push-forward operation be obtained. Importantly, this behavior differs from previous flow matching efforts where learning the appropriate vector field is possible with or without optimal transport (Albergo et al., 2023; Pooladian et al., 2023; Liu et al., 2022b; Tong et al., 2023a).

Therefore, because $q(y_0) = q(y_1)$ and static optimal transport is used in training, Section 3.3, the remainder disappears and $u_t(x|y)$ defined by Eq. (7) and $p_t(x|y)$ satisfy the continuity equation.

$$\begin{aligned}\frac{d}{dt}\left(p_t(x|y)\right) &= -\mathrm{div}_x\left(p_t(x|y)u_t(x|y)\right) - \cancelto{0}{u_t(y)}\nabla_y p_t(x|y) \\ &= -\mathrm{div}_x\left(p_t(x|y)u_t(x|y)\right)\end{aligned} \tag{A.2}$$

A.2 Equivalence of the Flow Matching Objective

Theorem 3.2 *Let $p_t(x|y) > 0$ for all $x \in \mathbb{R}^N$, $y \in \mathbb{R}^M$, $t \in [0,1]$ and $\mathcal{L}_{MCFM}(\theta) = \mathbb{E}_{t,p_t(x,y)}\|v_\theta(x,y,t) - u_t(x|y)\|_2^2$. Let α be a stationary, isotropic kernel depending only on $w = \|y_0 - y_1\|_2$, decaying to 0 as $w \to \infty$, and $\mathcal{C}^2$ in a neighborhood of 0 with $\alpha(0) = 1$ and $\alpha'(0) = 0$, and further assume the coupling $\pi(w)$ satisfies $\mathbb{E}_{\pi(w)}[\|y_0 - y_1\|_2^2] < \infty$. Then there exists a constant C such that for every θ,*

$$\left\|\nabla_\theta \mathcal{L}_{\mathrm{CVFM}}(\theta) - \nabla_\theta \mathcal{L}_{\mathrm{MCFM}}(\theta)\right\| \leq C\,\mathbb{E}\big[\|y_0 - y_1\|^2\big]. \tag{A.3}$$

If $\pi(w)$ enforces $\mathbb{E}_{\pi(w)}[\|y_0 - y_1\|_2^2] = O(\varepsilon^2)$ then the gradient error is $O(\varepsilon^2)$.

Proof. Several assumptions are necessary to guarantee the existence of various integrals and to allow exchanging of their order. Specifically, we assume $q(w,z)$, $p_t(x|z)$, $p_t(y|w)$ and $p(w)$ decrease to zero as $\|x\|, \|y\| \to \infty$ and that v_t, v_t, and $\nabla_\theta v_t$ are bounded. Furthermore, the optimal transport penalty, η, is taken to be sufficiently large such that when sampling in mini-batches approximating the optimal coupling between $q(y_0)$ and $q(y_1)$, $y_0 \approx y_1$. Additionally, we assume α is $\mathcal{C}^2$ in a neighborhood of 0 with $\alpha(0) = 1$ and $\alpha'(0) = 0$.

We begin by stating the intractable marginal conditional flow matching (MCFM) objective

$$\mathcal{L}_{\mathrm{MCFM}}(\theta) = \mathbb{E}_{t,p_t(x,y)}\|v_\theta(x,y,t) - u_t(x|y)\|^2 \tag{A.4}$$

Expanding the L_2-norm

$$\begin{aligned}\mathcal{L}_{\mathrm{MCFM}}(\theta) &= \mathbb{E}_{t,p_t(x,y)}\|v_\theta(x,y,t) - u_t(x|y)\|^2 \\ &= \mathbb{E}_{t,p_t(x,y)}\left[\underbrace{\|v_\theta(x,y,t)\|^2}_{T_1} - \underbrace{2\left\langle v_\theta(x,y,t), u_t(x|y)\right\rangle}_{T_1} + \underbrace{\|u_t(x|y)\|^2}_{T_3}\right]\end{aligned}$$

Consider each term independently. Note, the third term can be ignored because it is independent of the trainable parameters.

$$\begin{aligned}T_1 &= \mathbb{E}_{t,p_t(x,y)}\left[\|v_\theta(x,y,t)\|^2\right] \\ &= \mathbb{E}_t\left[\int p_t(x,y,w,z)\|v_\theta(x,y,t)\|^2 dz dw dx dy\right] \\ &= \mathbb{E}_t\left[\int p_t(x|z)p_t(y|w)q(z,w)\|v_\theta(x,y,t)\|^2 dz dw dx dy\right] \\ &= \mathbb{E}_{t,p_t(x|z),p_t(y|w),q(z,w)}\left[\|v_\theta(x,y,t)\|^2\right]\end{aligned}$$

Consider the second term.

$$
\begin{aligned}
T_2 &= -2\mathbb{E}_{t,p_t(x,y)}\left[\langle v_\theta(x,y,t), u_t(x|y)\rangle\right] \\
&= -2\mathbb{E}_t\left[\int p_t(x,y)\left\langle v_\theta(x,y,t), \int u_t(x|z)\frac{p_t(x,y|z,w)q(z,w)}{p_t(x,y)}dzdw\right\rangle dxdy\right] \\
&= -2\mathbb{E}_t\left[\int p_t(x,y)\frac{p_t(x,y|z,w)q(z,w)}{p_t(x,y)}\left\langle v_\theta(x,y,t), u_t(x|z)\right\rangle dxdydzdw\right] \\
&= -2\mathbb{E}_t\left[\int p_t(x|z)p_t(y|z)q(z,w)\left\langle v_\theta(x,y,t), u_t(x|z)\right\rangle dxdydzdw\right] \\
&= -2\mathbb{E}_{t,p_t(x|z),p_t(y|z),q(z,w)}\left[\langle v_\theta(x,y,t), u_t(x|z)\rangle\right]
\end{aligned}
$$

Combining these together and comparing them against the expanded form for $\mathcal{L}_{\text{CVFM}}(\theta)$, we clearly see that the $\mathcal{L}_{\text{MCFM}}(\theta)$ and $\mathcal{L}_{\text{CVFM}}(\theta)$ objectives are equivalent up until a constant independent of the training parameters, θ.

The above equality demonstrates equivalence in the absence of the kernel α, where the only difference between the two objectives is the multiplicative factor $\alpha(w)$ appearing in the complete CVFM objective. Consequently the gradient difference can be written in the form

$$
\nabla_\theta\mathcal{L}_{\text{CVFM}}(\theta) - \nabla_\theta\mathcal{L}_{\text{MCFM}}(\theta) = \mathbb{E}_{q(w)}\big[(\alpha(w)-1)h_\theta\big], \tag{A.5}
$$

where h_θ is the grouping of terms T_1 and T_2 from above, including the expectations over the remaining variables. By the uniform-boundedness assumption there exists $H < \infty$ with $|h_\theta| \le H$ for all relevant θ.

By hypothesis α is $\mathcal{C}^2$ in a neighborhood of 0 with $\alpha(0) = 1$ and $\alpha'(0) = 0$, so a second-order Taylor expansion about $w = 0$ yields

$$
\alpha(w) - 1 = \tfrac{1}{2}\alpha''(0)w^2 + r(w), \qquad r(w) = o(w^2) \text{ as } w \to 0. \tag{A.6}
$$

Substituting this expansion into the gradient identity and taking norms gives the bound

$$
\big|\nabla_\theta\mathcal{L}_{\text{CVFM}}(\theta) - \nabla_\theta\mathcal{L}_{\text{MCFM}}(\theta)\big| \le H\mathbb{E}_{q(w)}\big[|\alpha(w)-1|\big] \le H\Big(\tfrac{1}{2}|\alpha''(0)|\mathbb{E}_{q(w)}[w^2] + \mathbb{E}_{q(w)}[|r(w)|]\Big). \tag{A.7}
$$

Since $r(w) = o(w^2)$ is integrable pointwise, dominated convergence implies $\mathbb{E}_{q(w)}[|r(w)|] = o(\mathbb{E}_{q(w)}[w^2])$. Hence the right-hand side is $O(\mathbb{E}_{q(w)}[w^2])$, so there exists a constant C (depending only on H and $\alpha''(0)$) with

$$
\big|\nabla_\theta\mathcal{L}_{\text{CVFM}}(\theta) - \nabla_\theta\mathcal{L}_{\text{MCFM}}(\theta)\big| \le C\mathbb{E}_{q(w)}[w^2], \tag{A.8}
$$

which is the claimed inequality. The refined identity

$$
\nabla_\theta\mathcal{L}_{\text{CVFM}}(\theta) - \nabla_\theta\mathcal{L}_{\text{MCFM}}(\theta) = \tfrac{1}{2}\alpha''(0)\mathbb{E}_{q(w)}[w^2 h_\theta] + o(\mathbb{E}_{q(w)}[w^2]) \tag{A.9}
$$

shows that the linear term vanishes and the leading contribution is quadratic in w, so the approximation is exact to second order. Finally, if $\alpha \equiv 1$ then $\alpha(w) - 1 \equiv 0$ and the gradient difference vanishes identically.

A.3 Continuity of Conditional Flows

Theorem 3.3 *Let the learned vector field $v_\theta(x,y,t)$ be locally Lipschitz continuous with respect to both x and y. Let $\phi_t(x_0,y)$ be the path of a particle starting at x_0 generated by the ODE $\frac{dx}{dt} = v_\theta(x,y,t)$. Then, for any fixed $t \in [0,1]$ and initial distribution $p_0(x)$:*

1. *The transport map $\phi_t(x_0,\cdot)$ is continuous with respect to the conditioning variable y.*
2. *The pushforward probability measure $(\phi_t(\cdot,y))_\# p_0 = p_t(\cdot|y)$ is continuous with respect to y in the Wasserstein sense.*

Proof. Let y_1 and y_2 be two distinct conditioning variables. The corresponding paths are solutions to the integral equations:

$$\phi_t(x_0, y_i) = x_0 + \int_0^t v_\theta(\phi_s(x_0, y_i), y_i, s)\, ds \quad \text{for } i = 1, 2 \tag{A.10}$$

By the assumption that v_θ is locally Lipschitz continuous in both x and y, standard theorems on ODEs guarantee that the solution $\phi_t(x_0, y)$ is continuous with respect to the parameter y, proving the first claim.

The continuity of the pushforward measure follows from the continuity of the transport map. The squared Wasserstein-2 distance between the two pushforward measures is bounded by the expected squared distance between the paths:

$$W_2^2(p_t(\cdot|y_1), p_t(\cdot|y_2)) \leq \mathbb{E}_{x_0 \sim p_0(x)} \left[\|\phi_t(x_0, y_1) - \phi_t(x_0, y_2)\|^2 \right] \tag{A.11}$$

Since $\phi_t(x_0, y)$ is continuous in y for each x_0, as $y_2 \to y_1$, the right-hand side converges to 0 (assuming mild regularity conditions on p_0). Therefore, $p_t(\cdot|y)$ is continuous in y with respect to the Wasserstein distance, proving the second claim.

B Appendix: Additional Simulation-Free Score and Flow Matching Background

Tong et al. (2023a) proposed a simulation-free training objective for approximating continuous time Schrödinger bridges (Bunne et al., 2023a; De Bortoli et al., 2023), generalizing Flow Matching (FM) (Lipman et al., 2023; Albergo & Vanden-Eijnden, 2023) to the case of stochastic dynamics with arbitrary source distributions. Let $p : [0, 1] \times \mathbb{R}^N \to \mathbb{R}^+$ define a time-dependent probability path, $u : [0, 1] \times \mathbb{R}^N \to \mathbb{R}^N$ a time-dependent vector field, and $g : [0, 1] \to \mathbb{R}_{>0}$ a continuous positive diffusion function. An associated Itô stochastic differential equation (SDE) can be defined

$$dx = u_t(x)dt + g(t)dw_t \tag{B.1}$$

where $u_t(x)$ is equivalent to $u(t, x)$, and dw_t is standard Brownian motion. Utilizing the *Fokker-Planck equation* and *continuity equation*, it is possible to derive the *probability flow* ordinary differential equation (ODE) of the process (Tong et al., 2023a; Song et al., 2021) and comprise a relation between the probability flow ODE $\hat{u}_t(x)$ and the SDE drift as

$$u_t(x) = \hat{u}_t(x) + \frac{g^2(t)}{2} \nabla \log p_t(x). \tag{B.2}$$

As long as the probability flow ODE and score function can be specified, the SDE can be adequately described. Tong et al. (2023a) demonstrated that the intuition underpinning Eq. (6) can also be extended to the marginalization over conditional scores, resulting in the expressions

$$\begin{aligned} \hat{u}_t(x) &= \int \hat{u}_t(x|z) \frac{p_t(x|z)q(z)}{p_t(x)} dz \\ \nabla \log p_t(x) &= \int \nabla \log p_t(x|z) \frac{p_t(x|z)q(z)}{p_t(x)} dz. \end{aligned} \tag{B.3}$$

Gaussian marginal conditional flows: Prior works (Theorem 3 (Lipman et al., 2023), Theorem 2.1 (Tong et al., 2023b), Theorem 2.6, (Albergo & Vanden-Eijnden, 2023)) have demonstrated a method for tractably evaluating Eq. (B.3) in the case where the ODE/SDE conditional flows are Gaussian (i.e., $p_t(x|z) = \mathcal{N}(x; \mu_t(z), \sigma_t^2(z))$. The unique vector field $\hat{u}_t(x|z)$ generating this flow has the form

$$\hat{u}_t(x|z) = \frac{\sigma_t'(z)}{\sigma_t(z)}(x - \mu_t(z)) + \mu_t'(z) \tag{B.4}$$

where $\sigma_t'(z)$ and $\mu_t'(z)$ denote the time derivatives of $\sigma_t(z)$ and $\mu_t(z)$, respectively. This can seamlessly be extended to define the conditional score $\nabla \log p_t(x|z) = -(x - \mu_t(z))/\sigma_t^2(z)$. In the particular case of a

Brownian bridge from x_0 to x_1, sampled from $q(z)$, with constant diffusion rate $g(t) = \sigma$, the conditional flow is defined as $p_t(x|z) = \mathcal{N}(x; tx_1 + (1-t)x_0, \sigma^2 t(1-t))$, resulting in

$$\begin{aligned} \hat{u}_t(x|z) &= \frac{1-2t}{t(1-t)}(x - (tx_1 + (1-t)x_0)) + (x_1 - x_0) \\ \nabla \log p_t(x|z) &= \frac{tx_1 + (1-t)x_0 - x}{\sigma^2 t(1-t)}. \end{aligned} \tag{B.5}$$

In a similar manner to the derivation shown in Appendix A, a density over initial conditions $p(x_0)$, induces marginal distributions $p_t(x)$ satisfying the *Fokker-Planck equation* where $\Delta p_t = \nabla \cdot (\nabla p_t)$ (Tong et al., 2023a):

$$\frac{\partial p}{\partial t} = -\nabla \cdot (p_t u_t) + \frac{g^2(t)}{2} \Delta p_t \tag{B.6}$$

In total, Tong et al. (2023a) demonstrate that the concept of regressing upon the conditional vector field from FM can be extended to regressing upon conditional drift and score, providing improved performance in practice.

Weighting schedule $\lambda(t)$: In the case with conditional Gaussian $p_t(x|z)$ probability paths, as in Eq. (B.4), Tong et al. (2023a) advocate a particular weighting schedule $\lambda(t)$:

$$\lambda(t) = \frac{2\sigma_t}{\sigma^2} = \frac{2\sqrt{t(1-t)}}{\sigma}. \tag{B.7}$$

This weighting schedule provides simplification to the objective alongside numerical stability, converting the score matching objective to

$$\lambda(t)^2 \|s_\theta(x,t) - \nabla_x \log p_t(x|z)\|^2 = \|\lambda(t) s_\theta(x,t) + \varepsilon\|^2 \tag{B.8}$$

where $\varepsilon \sim \mathcal{N}(0,1)$.

C Appendix: Case Study Background

C.1 Microstructure Evolution in Materials Informatics

In this section, we provide a brief background of relevant topics for the third case study, describing relevant materials background at a high level. Appendix D and Appendix E provide more details on the datasets and empirical distributions involved in training as well as greater analysis of the case study results.

Phase-Field modeling: Phase-field simulations are commonly applied to model a number of manufacturing processes involving evolving interfaces (such as solidification/melting, spinodal decomposition, grain growth, recrystallization, and crack propagation (Steinbach, 2009; Miehe et al., 2010)). In particular, the Cahn-Hilliard equation is frequently used to describe spinodal decomposition, a spontaneous thermodynamic-instability-induced phase separation (Cahn & Hilliard, 1958). This partial differential equation models a diffusion driven process which minimizes the total energy of the system by inducing phase separation. In this work, we use the formulation described in Montes de Oca Zapiain et al. (2021); we use the standard Cahn-Hilliard equation with a double well potential describing the local contribution to the total energy Dingreville et al. (2020). The material state is represented using a single, continuous field variable, $c(x)$, that separates into two phases ($c = -1$ and $c = 1$).

$$\frac{\partial c}{\partial t} = \nabla \cdot \left(\mathcal{M}(c) \nabla \frac{\partial f(c)}{\partial c} - \kappa \nabla^2 c \right) \tag{C.1a}$$

$$f(c) = \omega (c-1)^2 (c+1)^2 \tag{C.1b}$$

$$\mathcal{M}(c) = s(c)\mathcal{M}_1 + \Big(1 - s(c)\Big)\mathcal{M}_2 \tag{C.1c}$$

$$s(c) = \frac{1}{4}(2-c)(1+c)^2 \tag{C.1d}$$

The values of the c field corresponding to each separated phase are defined by the minima of the chemical free energy density, $f(c)$. The spatially-dependent concentration field, $c(x)$, will take the role of material microstructure. The concentration dependent mobility, $\mathcal{M}(c)$, which defines the diffusion dynamics of the concentration field, $c(x)$, is parameterized by $\mathcal{M}_1$ and $\mathcal{M}_2$ which are scalar constant mobility parameters for each phase. Parameters ω and κ, the energy barrier height and the gradient energy coefficient, respectively, are both set to 1. For the purpose of modeling the system's stochastic dynamics using CVFM, the neural network is conditioned on three parameters: $\log(\mathcal{M}_1)$, $\log(\mathcal{M}_2)$, and c_0 – the initial concentration of the c field at time zero. We note that at time zero, $c(x) = c_0 + \epsilon(x)$, where $\epsilon(x)$ is a low variance, clipped white noise field (i.e., values cannot exceed $[-1, 1]$ after the sum) (e.g., $\text{STD}[\epsilon(x)] = 0.35$). This stochasticity is necessary to initiate phase separation and results in a distribution of final microstructures when a single set of $\mathcal{M}_1, \mathcal{M}_2, c_0$ are rerun several times. The dataset utilized in this paper's third presented case study was simulated under periodic boundary conditions using the MEMPHIS code base from Sandia National Labs (Dingreville et al., 2020). Details on the dataset are included in Appendix D.6.

2-Point spatial correlations: This work uses 2-point spatial correlations (Torquato, 2002; Kalidindi, 2015; Adams et al., 2013) as descriptive microstructure features to quantify the state of the material microstructure at a given time. This featurization builds on the idea that the microstructure itself is a stochastic function, where individual observed microstructure instances are simply samples from governing stochastic microstructure function (SMF) (Kröner, 1971; Torquato, 2002; Niezgoda et al., 2011). This concept was developed and is used to account for the observed degeneracy in material microstructures represented in direct space (e.g., for spinodal decomposition, represented directly as the concentration field, $c(x)$). This degeneracy refers to the observation that visually dissimilar microstructures sampled from the same underlying SMF are characterized by identical physical properties and process evolution in response to an applied environment. Therefore, it is more physically relevant (and computationally simple) to quantify evolution in SMFs than individual observed microstructures. Within this conceptualization, the underlying stochastic microstructure function is identified from individual instances by empirically estimating the moments of the SMF – e.g., its second order moments: the 2-point statistics. In practice, it is generally sufficient to represent material microstructures using their 2-point statistics. In addition to addressing degeneracy, a 2-point statistics based representation also provides a convenient mechanism to account for underlying symmetries (such as translation-equivariance and periodicity).

In practice, 2-point spatial correlations can be computed as a convolution of the sampled discrete microstructure function m_s^α, where α indexes the material local state and s indexes the spatial voxel. For the considered spinodal decomposition problem, $m_s = c_s$ has a one dimensional state. The resulting 2-point spatial correlations between two arbitrary material states, α and β, are then defined by the operation

$$f_r^{\alpha\beta} = \frac{1}{S} \sum_{s=1}^{S} m_s^\alpha m_{s+r}^\beta \tag{C.2}$$

where S is the number of voxels in the microstructural domain. Dimensionality reduction techniques can then be effectively applied to a dataset of 2-point spatial correlations to provide robust, information-dense features for the construction of linkages between process parameters and internal material structure (Gupta

et al., 2015; Latypov et al., 2019; Yabansu et al., 2020; Marshall & Kalidindi, 2021; Paulson et al., 2017; Generale & Kalidindi, 2021; Kalidindi, 2020; Harrington et al., 2022).

D Appendix: Experimental Details

D.1 Algorithm

In this section, we present the general algorithm for Conditional Variable Flow Matching given $q(z, w)$, $p_t(x|z)$, $p_t(y|w)$, and $u_t(x|z)$ in Algorithm 1, and the Schrödinger bridge extension with flow and score matching given $\nabla_x \log p_t(x|z)$ in Algorithm 2.

Algorithm 1 Conditional Variable Flow Matching

Require: Source and target data distributions $q(x_0, y_0)$ and $q(x_1, y_1)$ consisting of two unpaired sets of observed samples, noise hyperparameters σ_x, σ_y, mini-batch size B, and network v_θ.

while Training **do**

$\{(x_0, y_0), (x_1, y_1)\}_{b=1}^{B} \sim q(x_0, y_0), q(x_1, y_1)$ ▷ Sample empirical distributions of size B.

$\pi \leftarrow \mathrm{OT}(\{(x_0, y_0), (x_1, y_1)\}_{b=1}^{B})$ ▷ Interchangeable with Sinkhorn algorithm (Cuturi, 2013).

$t \sim \mathcal{U}(0, 1)$

$\{(x_0, x_1), (y_0, y_1)\}_{b=1}^{B} \sim \pi(z, w)$ ▷ Resample from OT coupling.

$z = \left[(x_0^{(1)}, x_1^{(1)}), \ldots, (x_0^{(B)}, x_1^{(B)})\right], \quad w = \left[(y_0^{(1)}, y_1^{(1)}), \ldots, (y_0^{(B)}, y_1^{(B)})\right]$

$\alpha(w) \leftarrow \exp(-\|y_0 - y_1\|_2^2 / 2\sigma_y^2)$ ▷ Evaluate kernel for sampled conditioning values.

$p_t(x|z) \leftarrow \mathcal{N}(x; tx_1 + (1-t)x_0, \sigma_x^2)$

$p_t(y|w) \leftarrow \mathcal{N}(y; ty_1 + (1-t)y_0, \sigma_y^2)$

$x_t \sim p_t(x|z)$

$y_t \sim p_t(y|w)$

$u_t(x|z) \leftarrow x_1 - x_0$

$\mathcal{L}_{\mathrm{CVFM}}(\theta) \leftarrow \mathbb{E}_{t, q(z,w), p_t(x,y|z,w)} \left[\alpha(w) \left\| v_\theta(x, y, t) - u_t(x|z) \right\|^2\right]$

$\theta \leftarrow \mathrm{Update}(\theta, \nabla_\theta \mathcal{L}_{\mathrm{CVFM}}(\theta))$

end while

return v_θ

D.2 Static Optimal Transport

Static exact and entropic regularized optimal transport couplings were solved for in mini-batches during training through the Python Optimal Transport (POT) package (Flamary et al., 2021) (`https://pythonot.github.io/`). As similarly reported in (Tong et al., 2023a), we noticed improved performance in the low-dimensional toy cases with the Sinkhorn algorithm (Cuturi, 2013), which degraded in higher dimensions (e.g., material dynamics, domain transfer). The use of mini-batch optimal transport has also been previously shown to regularize the transport plan (Fatras et al., 2021b;a) due to the stochastic nature of the independent batch samplings forming non-optimal couplings, in effect resulting in entropic-regularized OT plans, even with exact OT solves.

D.3 Computational Resources

All experiments were performed on a high-performance-computing cluster with CPU nodes of 24 CPUs and GPU nodes with V100 and A100 GPUs. 2D experiments were all performed on 1 V100, domain transfer and material dynamics experiments were performed on 4x V100's or 2x A100's.

D.4 2D Experimental Details

The 2D experiments involve three toy examples: 8 Gaussians-Moons, 8 Gaussians-8 Gaussians, and Moons-Moons. These simple case studies are meant to analyze the training stability of CVFM (and ablations

Algorithm 2 Conditional Variable Score and Flow Matching

Require: Source and target data distributions $q(x_0, y_0)$ and $q(x_1, y_1)$ consisting of two unpaired sets of observed samples, noise hyperparameters σ_x, σ_y, mini-batch size B, weighting schedule $\lambda(t)$, drift network v_θ, and score network s_θ.

while Training **do**

$\{(x_0, y_0), (x_1, y_1)\}_{b=1}^{B} \sim q(x_0, y_0), q(x_1, y_1)$ ▷ Sample empirical distributions of size B.

$\pi \leftarrow \text{Sinkhorn}(\{(x_0, y_0), (x_1, y_1)\}_{b=1}^{B}, 2\sigma_x^2)$

$t \sim \mathcal{U}(0, 1)$

$\{(x_0, x_1), (y_0, y_1)\}_{b=1}^{B} \sim \pi(z, w)$ ▷ Resample from OT coupling.

$z = \left[(x_0^{(1)}, x_1^{(1)}), \ldots, (x_0^{(B)}, x_1^{(B)})\right], \quad w = \left[(y_0^{(1)}, y_1^{(1)}), \ldots, (y_0^{(B)}, y_1^{(B)})\right]$

$\alpha(w) \leftarrow \exp(-\|y_0 - y_1\|_2^2)/2\sigma_y^2)$ ▷ Evaluate kernel for sampled conditioning values.

$p_t(x|z) \leftarrow \mathcal{N}(x; tx_1 + (1-t)x_0, \sigma_x^2)$

$p_t(y|w) \leftarrow \mathcal{N}(y; ty_1 + (1-t)y_0, \sigma_y^2)$

$x_t \sim p_t(x|z)$

$y_t \sim p_t(y|w)$

$u_t(x|z) \leftarrow ((1-2t)/(2t(1-t)))(x - (tx_1 + (1-t)x_0)) + (x_1 - x_0)$

$\nabla_x \log p_t(x|z) \leftarrow (tx_1 + (1-t)x_0 - x)/(\sigma_x^2 t(1-t))$

$\mathcal{L}_{\text{CVSFM}}(\theta) \leftarrow \mathbb{E}_{t, q(z,w), p_t(x,y|z,w)} \left[\alpha(w) \left(\|v_\theta(x, y, t) - u_t(x|z)\|^2 + \lambda(t)^2 \|s_\theta(x, y, t) - \nabla_x \log p_t(x|z)\|^2\right)\right]$

$\theta \leftarrow \text{Update}(\theta, \nabla_\theta \mathcal{L}_{\text{CVSFM}}(\theta))$

end while

return v_θ, s_θ

of CVFM), baseline CVFM's performance against alternative solutions, and provide a sufficiently low-dimensional setting to visualize and analyze the flow pathways. The next paragraphs detail the data generation process for the toy case studies. For all three, mini-batches were generated on the fly from new samples from the base distributions. In Figure E.1, the source distributions are labeled with blue samples and the target distributions are labeled with red samples.

The 8 Gaussians-Moons toy problem involves discrete conditioning that can take 8 individual values. Each condition value uniquely identifies one of the 8 Gaussians. The probability of each condition value was uniform. The two moons are each separated into 4 corresponding sections each. Each moon was separated by assigning a given sample to a select condition value dictated by the sample's relative angle with respect to the origin of the containing moon. Each moon was broken into 4 condition value groups based on 45° degree segments. As shown in Figure E.1, the individual Gaussians share condition value with a specific moon in an alternating pattern. This leads to a flow with greater bifurcations. During training, new samples are generated for each mini-batch. Samples from the 8-Gaussians and the moons (including both x-location in 2D space and condition value, y) are generated independently to construct a mini-batch sampling from $q_{\text{Gauss}}(x_0, y_0)$ and $q_{\text{moon}}(x_1, y_1)$.

The 8 Gaussians-8 Gaussians toy problem also involves discrete conditioning that can take 8 unique values. The probability of each condition value was uniform. Each set of Gaussians is arranged in a circle, Fig. E.1. A single unique condition value is assigned to each Gaussian in a given set. The condition value assignments for each set are offset from each other by a single place rotation. Empirically, we observed that the proximity of the two rings leads to a flow with strong coupling between x and y that is challenging to learn. Samples are generated on the fly in each mini-batch. Each ring is sampled independently (first the Gaussian index is sampled, and then x-coordinates are sampled). The outer ring is the source distribution: $q_{\text{outer}}(x_0, y_0)$ and $q_{\text{inner}}(x_1, y_1)$.

Finally, the Moons-Moons toy problem involves continuous conditioning. As shown in Figure E.1, the red target moons are rotated 90° degrees with respect to the blue source moons. The rotation is performed about the combined origin of the two moons in the source distribution. Continuous conditioning is assigned based on the absolute location of a sample. The same expression is used for both the source and target distributions: $y = (x_0 - 10)I_{[0,1]} + (1 - I_{[0,1]})(x_0 + 10)$. Here, x_0 refers to the 0 component of the 2D x

(not x at time 0 as has been used in the rest of the paper). $I_{[0,1]}$ denotes a binary indicator denoting which moon in the pair the sample came from. To generate the target distribution, samples are drawn from the source. Then, the sample conditional label is assigned based on the reported equation. The probability of each condition was defined implicitly by the sampling process. Finally, the samples are rotated 90° degree. Via these operations, samples within the mini-batch are drawn independently from distributions $q_{\text{M1}}(x_0, y_0)$ and $q_{\text{M2}}(x_1, y_1)$.

For all 2D synthetic dataset cases we used networks of four layers with width 128 and GELU activations (Hendrycks & Gimpel, 2023). Optimization was carried out with a constant learning rate of $1e-3$ and ADAM-W (Loshchilov & Hutter, 2019) over 10,000 steps and a batch size of 256, unless otherwise specified. Sampling was performed by integration with the adaptive step size `dopri5` solver and tolerances $\texttt{atol} = \texttt{rtol} = 1e-5$. Conditional probability paths $p_t(x|z)$ were defined with $\sigma_x = 0.1$, which was held constant throughout all cases. Values of η and σ_y for $p_t(y|w)$ were varied between discrete and continuous conditioning cases. In discrete conditioning cases (*8 Gaussian - 8 Gaussian* and *8 Gaussian - Moons*), $\sigma_y = 0.02$ and $\eta = 100$, whereas in the continuous conditioning case (*Moons - Moons*), $\sigma_y = 0.5$ and $\eta = 5$.

Empirical values of the Wasserstein-2 distance were evaluated through 2,048 samples simulated through the learned conditional vector fields and computed against an equivalent number of samples from the target distribution. The W_2 reported distance differs depending on cases with continuous or discrete conditioning. In the discrete case, we take the mean of the conventional W_2 distance across all conditioning classes

$$W_2(\hat{p}_1, q_1) = \mathbb{E}_{y\sim p(y)}\left[\left(\inf_{\pi\in\Pi(\hat{p}_1,q_1)}\int \|x_i - x_j\|^2 d\pi(x_i, x_j)\right)^{1/2}\right] \tag{D.1}$$

while in the continuous case, we incorporate the conditional ground cost as

$$W_2(\hat{p}_1, q_1) = \left(\inf_{\pi\in\Pi(\hat{p}_1,q_1)}\int \left[\|x_i - x_j\|^2 + \eta\|y_i - y_j\|^2\right] d\pi((x_i, y_i), (x_j, y_j))\right)^{1/2} \tag{D.2}$$

with $\eta = 1e5$. Both distances are computed between samples from the target distribution q_1, and samples from q_0 simulated forward to $t = 1$ as $\hat{p}_1$.

Similar to (Tong et al., 2023b;a) and (Shi et al., 2023), we also report the normalized path energy with a similar continuous/discrete split, either as the expected value across all classes in the discrete case, or with the cost as in Eq. (10). For brevity, we only repeat the normalized path energy with this latter formulation

$$\text{NPE}(q_0, \hat{p}_1) = \frac{\left|\mathbb{E}_{q_0(z,w)}\int \|v_\theta(x, y, t)\|^2 dt - W_2^2(q_0, \hat{p}_1)\right|}{W_2^2(q_0, \hat{p}_1)}. \tag{D.3}$$

This quantity provides a normalized measure for the deviation of the path energy learned by the model v_θ to that which would be optimal, equivalent to the squared Wasserstein-2 distance denoting constant velocity trajectories.

D.5 MNIST-FashionMNIST Experimental Details

The second case study analyzes the performance of CVFM on high dimensional problems. In particular, it analyzes whether training remains stable when using the scaling kernel, $\alpha(w)$, on high dimensional problems (see Appendix A for theoretical analysis of the scaling kernel $\alpha(w)$). In fact, we see that training stability improves – mirroring the conclusions from the toy examples – even for the high-dimensional setting. In this case study, we explore conditional domain transfer between the MNIST and FashionMNIST datasets. This is a discrete condition problem. Here, the goal is to map samples with a given condition in the MNIST dataset to samples with the same condition in the FashionMNIST dataset. As in every case study, independent empirical distributions represent the source and target distributions. In this case study, the source distribution is the MNIST dataset where x_0 are images and y_0 are digit assignments. Similarly, x_1

and y_1 are the images and class assignments in the FashionMNIST dataset. Before Mini-batch OT Coupling, samples are drawn independently from each marginal distribution. See Appendix E.3 for the results for this case study.

The MNIST-FashionMNIST domain transfer experiments utilized a UNet architecture developed by OpenAI (`https://github.com/openai/guided-diffusion/tree/main`). The network configuration utilized in this work consisted of 64 channels, with channel multiples of [1,2,2,2]. 4 heads of self-attention over 16 and 8 resolution were applied with 2 residual blocks. Optimization was carried out with cosine annealing of the learning rate from $1e-4$ to $1e-8$ and ADAM-W (Loshchilov & Hutter, 2019) with weight decay $1e-4$ for ranges of 3,750 - 10,000 epochs and batch size of 1024, or equivalently 220,000 - 590,000 steps. Conditional probability paths were constructed with $\sigma_x = 0.1$, $\sigma_y = 1e-3$, and mini-batch conditional OT was performed with $\eta = 10$ and $\eta = 1000$.

Unconditional FID scores (i.e., FID scores computed over the marginal distribution on x_1 to compare the target ground truth and the predicted target) were computed over 10,000 samples using *Clean-FID* (`https://github.com/GaParmar/clean-fid`). Conditional FID scores were computed using the same algorithm, however the calculation was restricted to a subset of the total samples with matching conditioning (1,000 samples per class). This methodology directly captures the distributional match in a conditional sense, with ground truth target samples corresponding to a given condition are compared against samples from the source distribution with the same condition that had been evolved through time using the learned network. LPIPS scores were computed using *torchmetrics* (`https://github.com/Lightning-AI/torchmetrics`).

D.6 Material Dynamics Experimental Details

The final case study analyzes the performance of the proposed CVFM algorithm on our target scientific application: modeling the stochastic dynamics of a materials manufacturing process. Unlike the previous examples, the time variable now represents real time in the manufacturing process. In addition, the learned flow passes through a long sequence of empirical intermediate distributions instead of just two boundary distributions.

We use a dataset generated via spinodal decomposition simulations in MEMPHIS (Dingreville et al., 2020), see Appendix C. The dataset contains simulations of the evolution pathway (i.e., trajectory) of 10,000 two-phase microstructures of size 256×256 pixels. Each simulation is associated with mobility parameters $\mathcal{M}_1$ and $\mathcal{M}_2$, sampled according to the log-uniform $\log(\mathcal{M}) \sim \mathcal{U}(\log(0.1), \log(100))$, and an initial concentration $c_0 \sim \mathcal{U}(-0.7, 0.7)$. These processing parameters correspond to the mobility parameters of the two constituents $(\mathcal{M}_1, \mathcal{M}_2)$, and initial relative concentrations (c_0). Each microstructure's trajectory contains 100 sequential recorded frames representing the microstructure state at a given time (therefore, there are 1M total microstructures spanning 100 time steps). The dataset is split into $8,000$ training trajectories and $2,000$ testing trajectories. The microstructure state at any given time was represented using principal component-based dimensionality reduction of the 2-point statistics, Appendix C. The Principal Component Analysis basis was established based on the complete training dataset. All models were trained to evolve the coefficients of the first 5 PC dimensions.

We note that while complete trajectories for a given $(\mathcal{M}_1, \mathcal{M}_2, c_0)$ are available (and, therefore, paired data is available), the paired data is not utilized in training in order to simulate expected conditions in envisioned experimental applications. The complete trajectories are only used to compute error metrics in testing and to compare against standard methods (such as Neural ODE (Chen et al., 2018) and LSTM (Hochreiter & Schmidhuber, 1997)) that require paired data for training. Instead, state and conditioning pairs are randomly shuffled within each recorded frame in the dataset. They are combined together into joint distributions conditioned on time, $q_{mat}(x, y|\tau)$. Here, x is the PC coefficients representing the microstructure state. $y = (\log(\mathcal{M}_1), \log(\mathcal{M}_2), c_0)$ is the condition vector containing the mobilities and initial concentrations. τ is the absolute time of the sampled frame. For our example, this empirical distribution contains $800,000$ sample triplets. During training, minor adjustments are made to the underlying CVSFM algorithm (Algorithm 2) to account for the presence of multiple discrete time marginal distributions. Specifically, within each step we first sample a tuple of adjacent time pairs $(\tau_0, \tau_1) \sim \{(\tau_i, \tau_{i+1}\}_{i=0}^{T=99}$. Given this time pair, a mini-batch

of size $2B$ (x, y) tuple is drawn for each of these adjacent times. Each time-adjacent mini-batch is then resampled according to the empirical OT coupling (i.e., samples are drawn from the mini-batch estimate of the optimal coupling). Lastly, the standard CVFM algorithm is adjusted such that $t \sim \mathcal{U}(0, 1)$ and then linearly mapped to $\tau = \tau_0 + t(\tau_1 - \tau_0)$ where $\tau \in [\tau_0, \tau_1]$. This complete CVSFM algorithm for stochastic dynamics is outlined in Algorithm 3.

Algorithm 3 Time-Specific Conditional Variable Score and Flow Matching for Stochastic Dynamics

Require: Source and target data distributions $q(x_0, y_0)$ and $q(x_1, y_1)$ consisting of two unpaired sets of observed samples, noise hyperparameters σ_x, σ_y, mini-batch size B, weighting schedule $\lambda(t)$, drift network v_θ, and score network s_θ.

while Training **do**

$(\tau_0, \tau_1) \sim \{(\tau_i, \tau_{i+1})\}_{i=0}^{T=99}$ ▷ Randomly select adjacent times.

$\{(x_0, y_0), (x_1, y_1)\}_{b=1}^{B} \sim q(x_0, y_0|\tau_0), q(x_1, y_1|\tau_1)$

$\pi \leftarrow \mathrm{OT}(\{(x_0, y_0), (x_1, y_1)\}_{b=1}^{B})$ ▷ Interchangeable with Sinkhorn algorithm (Cuturi, 2013).

$\{(x_0^{(b)}, x_1^{(b)}), (y_0^{(b)}, y_1^{(b)})\}_{b=1}^{B} \sim \pi(z, w)$ ▷ Resample from time-specific OT coupling.

$t \sim \mathcal{U}(0, 1)$

$\tau \leftarrow \tau_0 + t(\tau_1 - \tau_0)$

$z = \left[(x_0^{(1)}, x_1^{(1)}), \ldots, (x_0^{(B)}, x_1^{(B)})\right], \quad w = \left[(y_0^{(1)}, y_1^{(1)}), \ldots, (y_0^{(B)}, y_1^{(B)})\right]$

$\alpha(w) \leftarrow \exp(-\|y_0 - y_1\|_2^2 / 2\sigma_y^2)$ ▷ Evaluate kernel for sampled conditioning values.

$p_t(x|z) \leftarrow \mathcal{N}(x; tx_1 + (1-t)x_0, \sigma_x^2 t(1-t))$

$p_t(y|w) \leftarrow \mathcal{N}(y; ty_1 + (1-t)y_0, \sigma_y^2 t(1-t))$

$x_t \sim p_t(x|z)$

$y_t \sim p_t(y|w)$

$u_t(x|z) \leftarrow ((1-2t)/(2t(1-t)))(x - (tx_1 + (1-t)x_0)) + (x_1 - x_0)$

$\nabla_x \log p_t(x|z) \leftarrow (tx_1 + (1-t)x_0 - x)/(\sigma_x^2 t(1-t))$

$\mathcal{L}_{\mathrm{CVSFM}} \leftarrow \mathbb{E}_{t, q(z,w), p_t(x,y|z,w)} \left[\alpha(w) \left(\|v_\theta(x, y, \tau) - u_t(x|z)\|^2 + \lambda(t)^2 \|s_\theta(x, y, \tau) - \nabla_x \log p_t(x|z)\|^2\right)\right]$

$\theta \leftarrow \mathrm{Update}(\theta, \nabla_\theta \mathcal{L}_{\mathrm{CVSFM}})$

end while

return v_θ, s_θ

Mean absolute error values, along with minimum and maximum absolute error reported in Table 2 were evaluated on a test set of 2,000 microstructures, and a training set of 8,000 microstructures. Known state was compared against the expectation of the predicted conditional distribution over the state variable at a given time $\mathbb{E}[x_t|x_0, y]$.

All material specific cases used networks with five layers of width 256 and GELU activations (Hendrycks & Gimpel, 2023). Skip connections were applied over the middle three layers. The conditioning variable was subject to both self-attention and time cross-attention with an embedding dimensionality of 64 and 8 heads. The same network architecture was used in T-COT-FM, and for both drift and score networks in CVSFM, COT-SFM, and T-COT-SFM. It was duplicated for the NeuralODE benchmark. The LSTM benchmark consisted of four layers with width 512 for approximately equivalent parameterization. Optimization was carried out with cosine annealing of the learning rate from $1e-3$ to $1e-8$ and ADAM-W (Loshchilov & Hutter, 2019) with weight decay $1e-2$ and an effective batch size of 1024. Conditional probability paths were constructed with $\sigma_x = 0.1$, $\sigma_y = 0.1$, and mini-batch conditional OT was performed with $\eta = 100$. While, T-COT-FM in it's initial formulation does not include a varying noise schedule across the conditioning variable, we have also included an ablation with this extension, mirroring the same value of σ_y.

E Appendix: Additional Case Study Specific Results

We move on towards presenting additional results obtained throughout this work. The results expand upon the discussion presented in Section 4 towards interrogating the empirical performance of CVFM, illuminating the critical advances necessary for learning conditional vector fields. We refer the reader to Appendix D for detailed descriptions of the datasets and training infrastructure used in each case study.

E.1 2D Experiments

In Figure 3 trajectories of the learned vector fields were presented for the *8 Gaussian - Moons* mapping with discrete conditioning and the *Moons - Moons* with continuous conditioning, although this remains a fraction of the cases run. For completeness, we present the trajectories of all methodologies evaluated in Table 1 in Figure E.1.

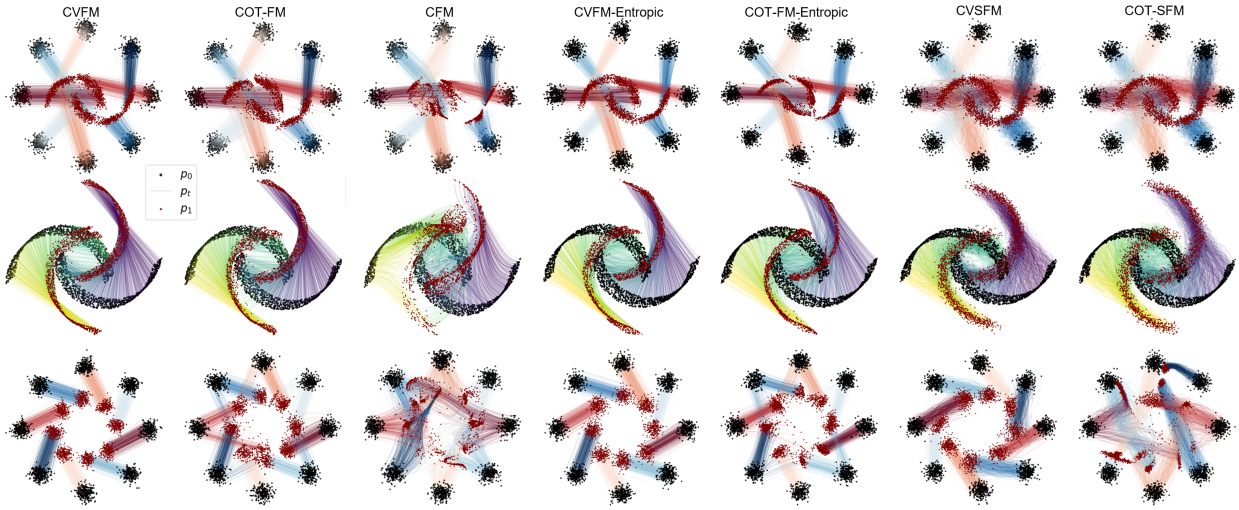

Figure E.1. Comparison of obtained trajectories for various OT and SB modeling approaches in the synthetic datasets considered associated with Wasserstein-2 error and normalized path energy reported in Table 1. Trajectories are colored by the conditioning variable. Source distributions are shown in black, target distributions are shown in maroon.

While, perhaps visually the simplest, the *8 Gaussian - 8 Gaussian* mapping, consisting of a 45 degree rotation about the origin, is demonstrably the most complex family of conditional vector fields to learn given samples of the empirical distribution $q(w, z)$. This is the only case in which only CVFM variants reliably learn to disentangle the conditional dynamics (Figure E.1), while COT-FM attempts to split mass to minimize transport costs across the joint $\mathcal{X} \times \mathcal{Y} : \mathbb{R}^N \times \mathbb{R}^M$, visualized by splits mapping to target densities with similar conditioning values.

Conditional Transport Cost: This mass splitting observed in the *8 Gaussian - 8 Gaussian* with COT-FM, alongside observed biasing effects in the *8 Gaussian - Moons* and *Moons - Moons* cases is a direct result of conditional transport cost defined in Eq. (10). The role of η in penalizing transport in the conditioning variable specifically dictates performance of the learned mappings of both COT-FM and CVFM, although has a more pronounced impact on the former. Additional ablations across all 2D cases can be seen in Figure E.2. Across all cases, a Wasserstein-2 error gap can be observed with the exception of *8 Gaussian - Moons* with $\eta > 25$. This only further reinforces earlier insights, highlighting the improved robustness of CVFM.

E.2 Supplementary Analysis of Estimator Variance

Conditioning Mismatch Kernel: The conditioning mismatch kernel $\alpha(w)$ plays a pivotal role in the objective introduced in Eq. (8), which we duplicate here in its complete form.

$$\mathcal{L}_{\text{CVFM}}(\theta) = \mathbb{E}_{t,q(z,w),p_t(x|z)p_t(y|w)} \left[\alpha(w)\|v_\theta(x, y, t) - u_t(x|z)\|^2\right] \tag{E.1}$$

The selected form of this kernel dictates the degree of continuity expected *a priori* in the observed joint vector fields $u_t(x, y)$ across $y \in \mathbb{R}^M$, introducing an inductive bias in the solution across this joint space, even if we only ever expect to evaluate the vector field in a conditional sense. In this work, we select the

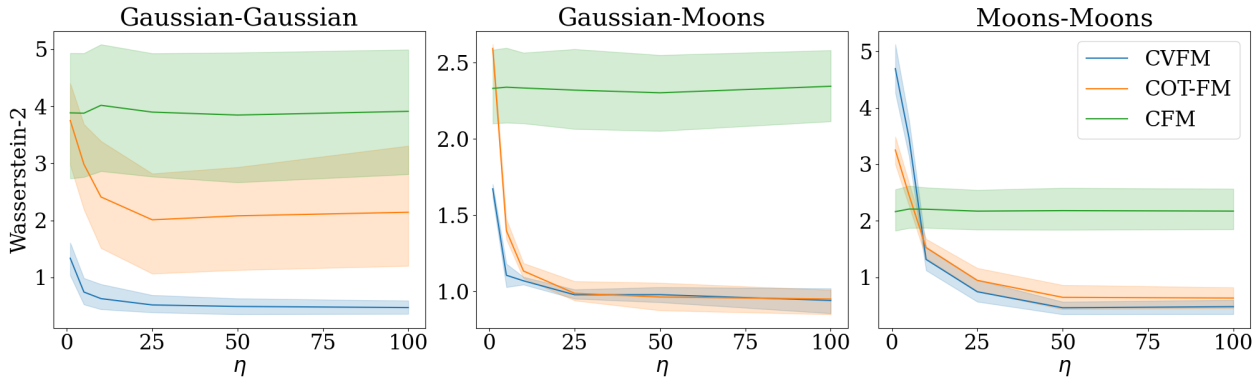

Figure E.2. Comparison of obtained trajectories for various OT and SB modeling approaches in the synthetic datasets considered associated with Wasserstein-2 error and normalized path energy reported in Table 1. Trajectories are colored by the conditioning variable. Source distributions are shown in black, target distributions are shown in maroon.

Squared Exponential (SE) kernel $\alpha(w) = \exp(-\|w\|_2^2/2\sigma_y^2)$ with observation $w = y_1 - y_0$, where the degree of continuity in u_t across the conditioning variable can be tailored through an appropriate selection of σ_y.

Previously, in Table 1, we observed significantly improved performance with the introduction of this additional modulation – which naturally raises questions as to its contribution in isolation. Figure E.4 demonstrating that even by itself in the absence of mini-batch OT, the introduction of $\alpha(w)$ is able to reliably equal or improve upon Wasserstein-2 target distribution error in comparison with COT-FM and CVFM. Figure E.5 similarly shows an evaluation across η values (the weighting in the optimal transport ground cost), highlighting the stability it introduces across all test cases relative to mini-batch OT solves with Eq. (10). In the *8 Gaussian - 8 Gaussian* case, $\alpha(w)$ drastically outperforms COT-FM, with comparable performance in the other mappings, albeit without providing approximate OT within the conditioned vector fields. Due to this limitation, one might view $\alpha(w)$ in isolation as a reliable extension to conditional CFM.

Objective Target Variance: One reason for the improved convergence of CVFM is the significantly lower variance of the training objective target in CVFM in comparison to similar existing methods such as COT-FM Kerrigan et al. (2024); Chemseddine et al. (2024). As discussed in Section 3.3, we measure this variance using the objective target variance (OTV):

$$\text{OTV} = \mathbb{E}_{t,q(z,w),p_t(x,y|z,w)}\|u_t(x|z)\|^2 \tag{E.2}$$

Notably, the absolute computed OTV values generally should not be compared across different test case studies because these equations are not normalized to the scale of the true underlying conditional vector field. Figure E.3 visualizes the relative reduction in variance as a function of batch size. As discussed in Section 3.3, the kernel leads to consistent reductions in variance across all applications. In practice, this characteristic is immensely valuably because it combats the well known instability of flow matching training, effectively reducing the number of necessary training steps (e.g., see Figure 3). In Figure E.3 we see that this reduction is remarkably consistent across batch sizes (e.g., the kernel achieves a reduction of roughly 90% for the challenging *Gaussian – Gaussian* topology). This indicates that the kernel continues to provide benefits even when other variance reduction methods are used as well. Table E.1 details the raw variance values, highlighting that while the *percentage* improvement is constant, the *absolute* stability gain is most critical in sparse regimes (e.g., reducing target variance from $77.38 \to 6.47$ at $B = 16$).

Kernel Sensitivity Ablation: While the results above demonstrate the utility of the SE kernel, a natural question arises regarding the sensitivity of CVFM to the specific functional form of $\alpha(w)$. To address this, we evaluated three kernels with distinct tail behaviors to test the robustness of the variance reduction mechanism:

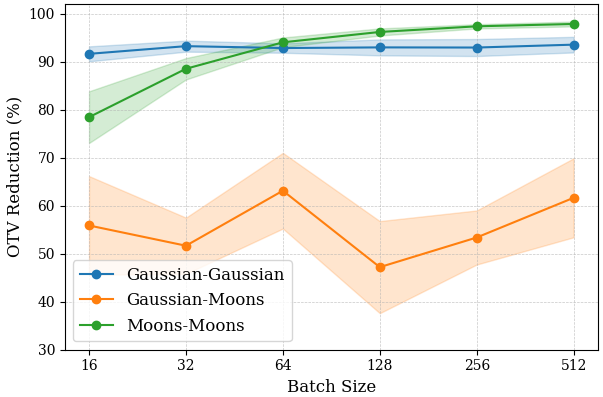

Figure E.3. Percentage reduction in variance achieved by CVFM relative to COT-FM. Across all batch sizes, the inclusion of the kernel $\alpha(w)$ consistently eliminates a significant portion of the estimator variance. Notably, in the *8 Gaussian–8 Gaussian* topology, which features the strongest conditional dependence, CVFM reduces variance by over 90% regardless of the sampling sparsity.

	Batch Size	8 Gaussian - 8 Gaussian	8 Gaussian - Moons	Moons - Moons
CVFM	16	6.465±0.561	7.847±1.405	0.699±0.157
	32	2.896±0.364	3.618±0.142	0.179±0.030
	64	1.515±0.200	1.648±0.268	0.044±0.007
	128	0.678±0.052	0.946±0.099	0.014±0.002
	256	0.379±0.086	0.493±0.057	0.005±0.001
	512	0.175±0.032	0.216±0.043	0.002±0.000
COT-FM	16	77.376±12.805	17.780±2.657	3.243±0.356
	32	42.891±4.948	7.482±0.857	1.561±0.154
	64	21.197±0.802	4.468±0.621	0.739±0.043
	128	9.672±2.178	1.791±0.266	0.369±0.049
	256	5.383±0.588	1.057±0.037	0.191±0.026
	512	2.718±0.475	0.563±0.045	0.094±0.012

Table E.1. Variance of the conditional objective across synthetic datasets swept across varying batch sizes. Variance values were computed over 5 seeds with a conditioning transport weight of $\eta = 10$. Values are reported as $\mu \pm \sigma$.

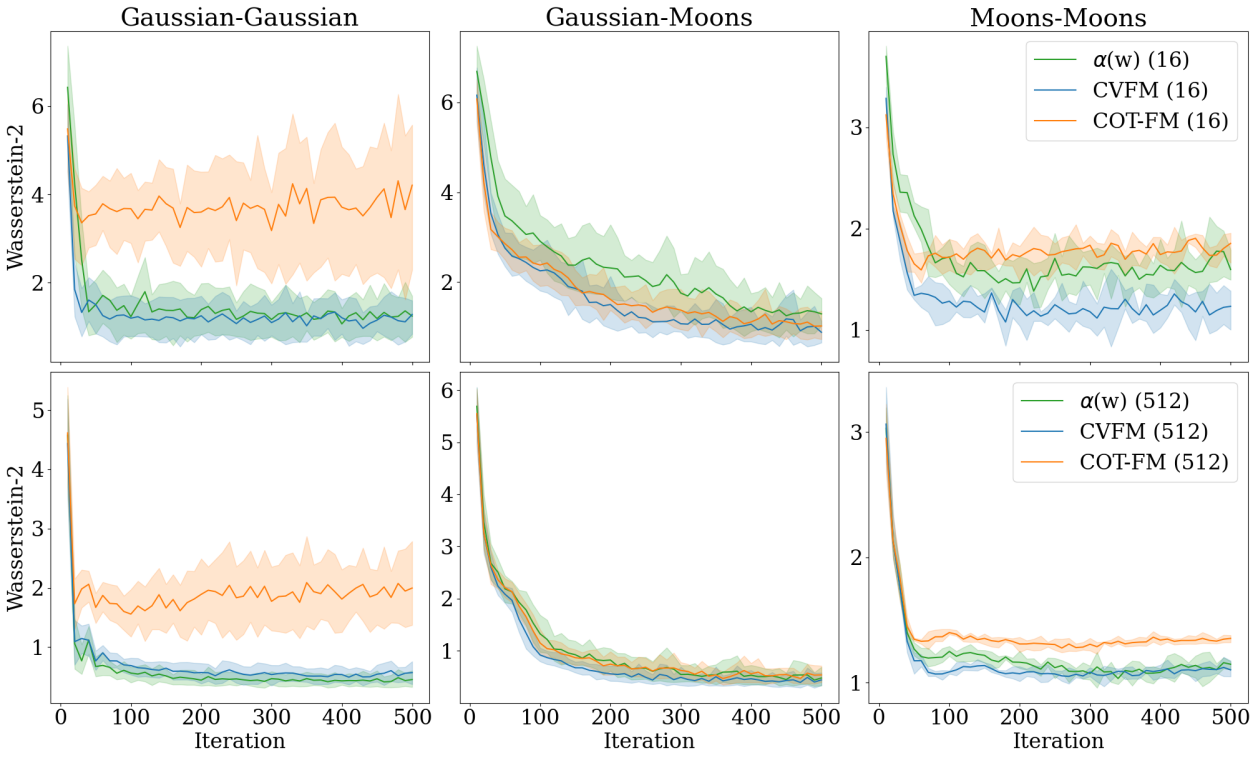

Figure E.4. Demonstration of the effectiveness of performing an expectation of the objective with solely $\alpha(w)$ in comparison to the COT-FM and CVFM approaches. The use of $\alpha(w)$ in isolation is better able to disentangle associated conditioning variables in almost all cases than the conditional Wasserstein distance introduced in Eq. (10).

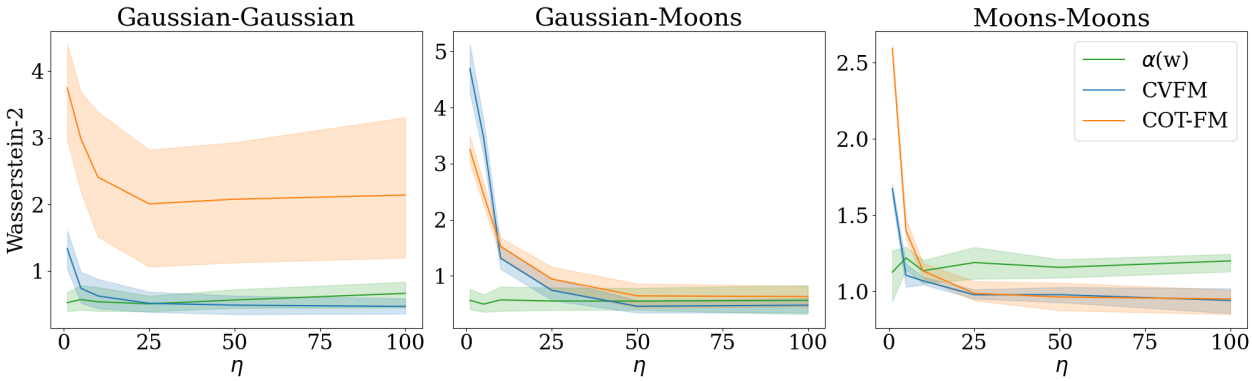

Figure E.5. $\alpha(w)$ more reliably reduces Wasserstein-2 error to the target distribution in comparison with COT-FM across values of η.

$$\text{Squared Exponential (light-tailed)}: \quad \alpha_{\mathrm{SE}}(w) = \exp\left(-\frac{\|w\|_2^2}{2\sigma^2}\right),$$

$$\text{Laplace (moderate tails)}: \quad \alpha_{\mathrm{Lap}}(w) = \exp\left(-\frac{\|w\|_1}{\sigma}\right),$$

$$\text{Cauchy (heavy-tailed)}: \quad \alpha_{\mathrm{Cauchy}}(w) = \left(1 + \frac{\|w\|_2^2}{\sigma^2}\right)^{-1}.$$

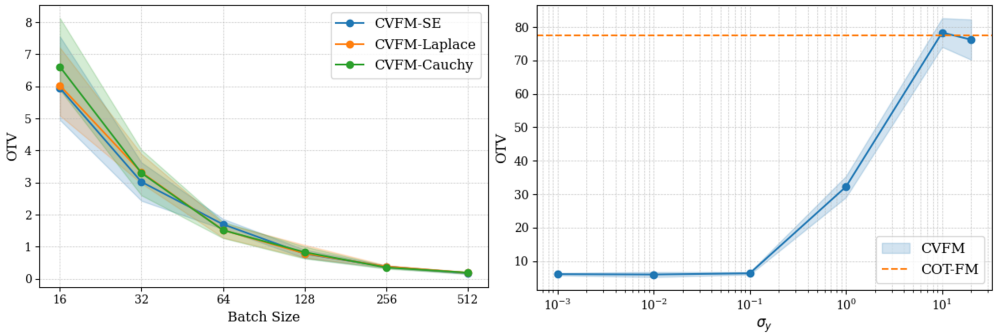

Figure E.6. Comparison of the three ablated kernels (left), and ablation of kernel bandwidth for the SE kernel (right) on the *8 Gaussian - 8 Gaussian* topology with $B = 16$ and $\eta = 10$, highlighting the robust variance reduction across varied bandwidths.

As shown in the left portion of Figure E.6, the choice of kernel has a measurable but minor impact on estimator stability compared to the baseline. The ordering of variance corresponds to the kernel's decay for a fixed bandwidth. The Squared Exponential (SE) kernel achieves the lowest variance due to its rapid decay and strict locality, suppressing noisy, distant pairings. The Cauchy kernel, with its heavy tails, allows more distant conditioning pairs to contribute to the gradient; while this increases the effective sample size, it introduces slightly more variance. However, the tight clustering of all three variants confirms that the method is robust: provided that *any* monotonically decaying kernel is used to enforce local consistency, the catastrophic variance explosion of COT-FM displayed in Figure 2 is avoided. The right portion of Figure E.6 demonstrates the impact of the SE's kernel bandwidth hyperparameter on target variance – highlighting the exceptional stability across a wide range spanning orders of magnitude relative to the COT-FM baseline.

Beyond empirical performance, the squared-exponential (SE) kernel is a natural choice from the perspective of entropic optimal transport (EOT). In EOT, the entropic regularization of the Kantorovich problem yields

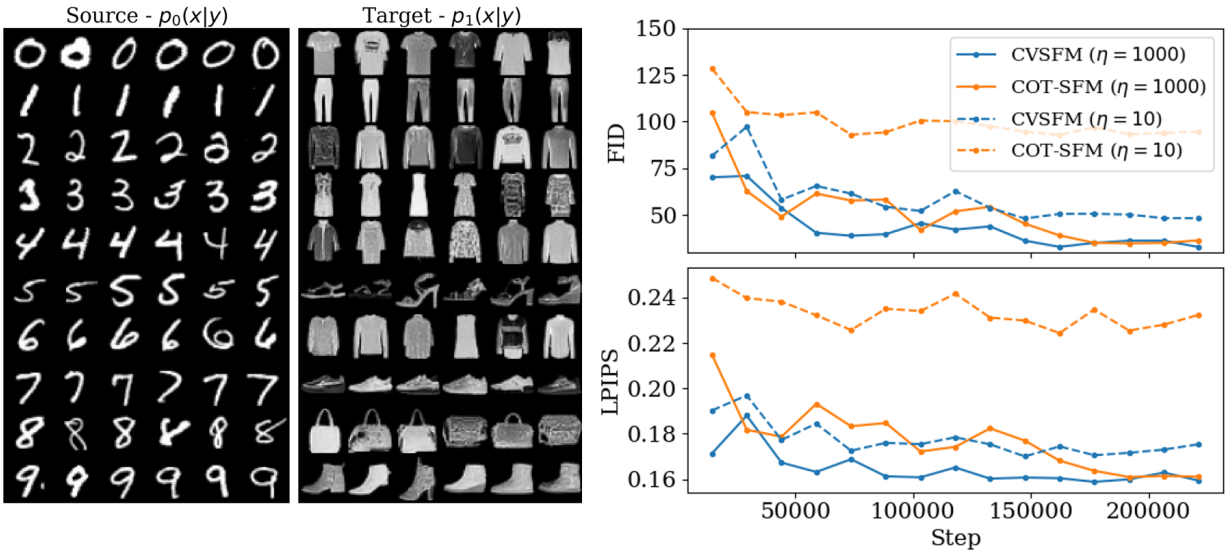

Figure E.7. CVSFM conditionally generated images from the FashionMNIST dataset. (Left) pane displays samples from the initial distributions $p_0(x|y)$, while the middle displays generated samples from $p_1(x|y)$. Relative positioning indicates paired samples. (Right) pane illustrates the improved convergence of CVSFM over COT-SFM in high-dimensional domain transfer for $\eta = 10$ and $\eta = 1000$. Displayed FID/LPIPS scores are computed per class and averaged.

transport plans of Gibbs form

$$\pi_\varepsilon \propto \exp\left(-\frac{C(y_0, y_1)}{\varepsilon}\right). \tag{E.3}$$

When the ground cost is the squared Euclidean distance $C(y_0, y_1) = \|y_0 - y_1\|_2^2$, the Gibbs factor is Gaussian in the vector difference $y_0 - y_1$, and thus an SE kernel $\alpha(y_0, y_1) \propto \exp(-\|y_0 - y_1\|^2/(2\sigma^2))$ arises (with $\sigma^2 = \varepsilon/2$, up to normalization). This provides a principled link between SE weighting and a soft, entropically-regularized preference for local conditioning. By contrast, heavy-tailed or non-smooth kernels (for example Cauchy or Laplace) do not correspond to the Gibbs factor for the squared-L_2 cost; (Laplace kernels do correspond to an L_1 cost, while Cauchy kernels cannot be written as a simple Gibbs factor of a quadratic cost). This observation plausibly explains the weaker variance reduction we observed for those kernels in our ablation. We therefore present the SE kernel as a theoretically motivated default, while still reporting improvements over COT-FM when other kernels are used.

E.3 MNIST-FashionMNIST Domain Transfer

In this section, we evaluate our method in high-dimensional domain transfer between MNIST digits and FashionMNIST clothing articles with conditioning by discrete class, illustrating the methodologies performance in higher dimensional distributional mappings. We directly compare our two variants, CVSFM against COT-SFM, Figure E.7. The FID and LPIPS scores reported are averages across the class conditioned scores (i.e., FID and LPIPS are computed on a per-class basis across 1,000 samples in each class). Select images from the source and corresponding generated images from the target conditional distributions are also shown. As seen in the repeated samples, the model is able to consistently map to the correct paired conditional distribution while displaying appreciable diversity within each class. Mirroring the 2D experiments, we observe improved convergence and mode coverage with CVSFM compared to COT-SFM across all η values due to $\alpha(w)$ modulating conditional flow.

This improved convergence with increasing η of COT-FM only further reinforces the value of ground cost scaling across y. Unfortunately, the optimal value of η is problem dependent, and is particularly challenging to identify a priori. The conditional scaling kernel ameliorates these difficulties. As shown in Figure E.3,

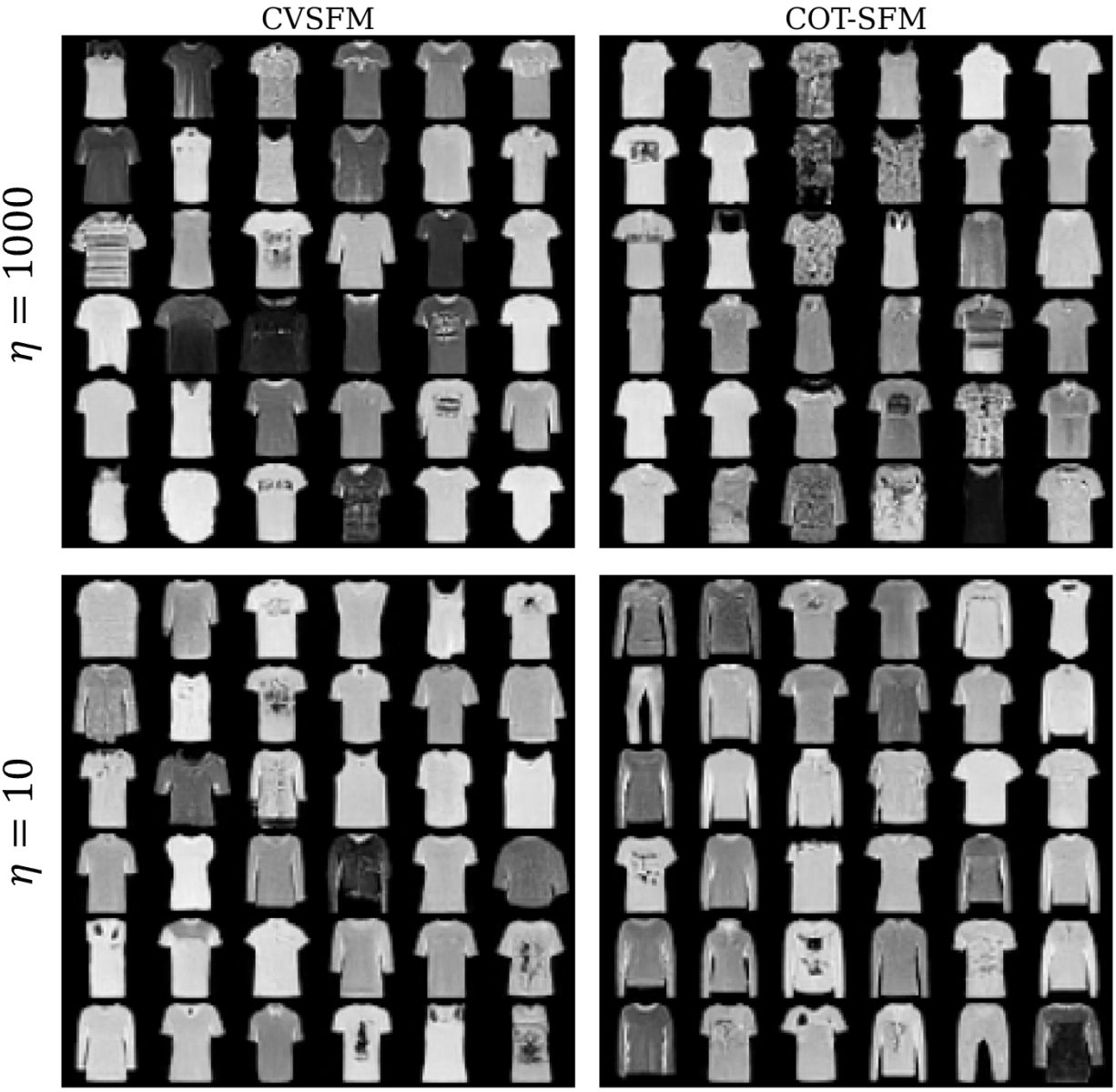

Figure E.8. Comparison of 32 randomly generated images corresponding to the first class of FashionMNIST with CVSFM and COT-SFM for $\eta = 10$ and $\eta = 1000$.

the kernel significantly reduces the objective variance in comparison with purely conditional OT, facilitating stable convergence and more accurate conditional mappings. This behavior was first observed in 2D examples in Figures 3 and E.1 and such characteristics extend to the high-dimensional setting. This increased stability facilitates a greater tolerance on η values, ameliorating potential difficulties during hyperparameter optimization. In Figure E.8, we observe this stability through the inspection of randomly generated samples from mapping the first class of MNIST to the first class of FashionMNIST. While in an unconditional sense, COT-SFM with $\eta = 10$ is able to appropriately transfer between MNIST and FashionMNIST, its consistency in mapping to the correct conditional distribution is lost without elevated penalization in transport across y. In comparison, CVSFM is able to consistently map to t-shirts/tops in the first class even with orders of magnitude difference in η. Similarly, in Figure E.7, the convergence behavior for CVFM degrades very little with large changes in η.

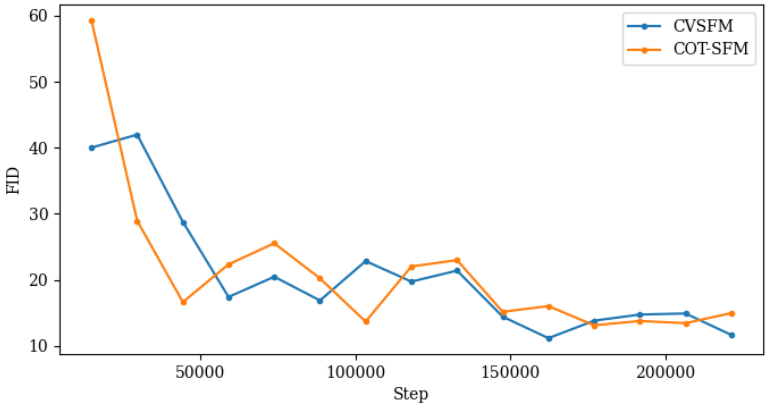

Figure E.9. Unconditional FID scores evaluated across 10,000 samples $x \sim p_1(x)$ for COT-SFM and CVSFM ($\eta = 1000$) during training.

Table E.2. Comparison of conditional mean (FID) and unconditional FID scores (FID-All) for 10,000 samples alongside conditional LPIPS scores.

Model	FID-All (↓)	FID (↓)	LPIPS (↓)
CVSFM ($\eta = 1000$)	11.668	32.915	0.159
COT-SFM ($\eta = 1000$)	14.965	36.456	0.161
CVSFM ($\eta = 10$)	23.554	48.326	0.175
COT-SFM ($\eta = 10$)	15.751	94.690	0.232

Figure E.7 displayed the convergence characteristics of conditional FID and LPIPS scores, conditionally evaluated for each class of $p_1(x|y)$, only serving to reinforce the prior discussion. In comparison, in evaluating FID scores for $p_1(x) = \int p_1(x|y)p(y)dy$, distinctions in the performance between CVSFM and COT-SFM are removed. Figure E.9 highlights the equivalence in unconditional performance in this case study across 10,000 images. This discrepancy in conditional to unconditional FID scores highlights limitations of mini-batch sampling from the conditional OT coupling $\pi_\eta((x_0, y_0), (x_1, y_1))$. Even with elevated weighting on transport in the conditioning variable, mini-batch conditional OT provides a poorer approximation.

E.4 Material Dynamics

The mean absolute error metrics displayed in Table 2 provide point estimates of the performance of our proposed method, providing evidence that we are capable of reliably disentangling the latent processing dynamics of material microstructures across the conditional processing space, given unpaired samples of process conditions and material state observed at discrete times. For further interrogation, we present the estimated error distributions in Figure E.10 across all 2,000 material samples in the test set. In congruence with the results presented earlier, CVSFM-exact outperforms all other methods, a surprising fact given the stochastic nature of only viewing observations sampled from $q(z, w, \tau)$. The Neural ODE (Chen et al., 2018) outperforms other methods, approximately matching the performance of the most optimal CVSFM-Exact variant (i.e., exhibiting similar tails and a mean shift). Figure E.11 compares the dynamics predicted by the three models on several selected members of the test dataset. Mirroring the distribution of errors in Figure E.10, the CVSFM model slightly outperforms the other two while also providing uncertainty estimates. The panels in Figure E.11 display the dynamics projected onto individual principal component subspaces, α_i.

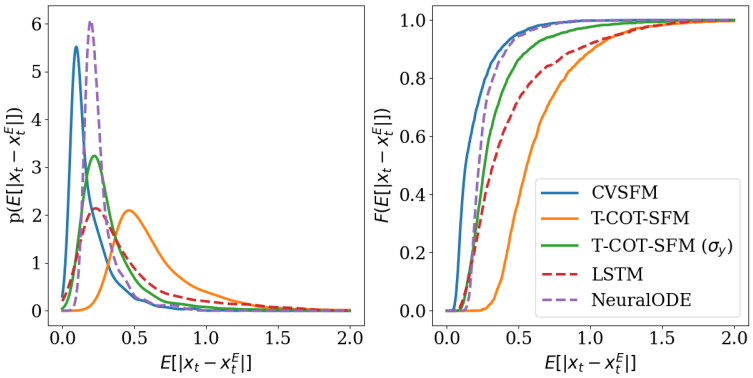

Figure E.10. (Left) probability density function, and (right) cumulative distribution function of CVFM in comparison with evaluated conventional approaches requiring complete trajectory information.

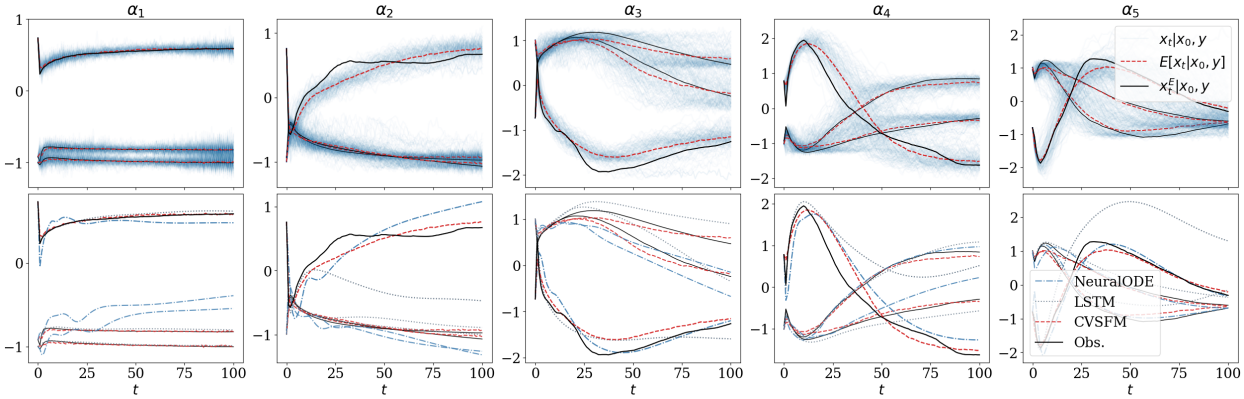

Figure E.11. Collection of three randomly sampled trajectories from the test set in PC space displaying (top) 128 samples in blue from CVSFM, with the expected value in red, and (bottom) deterministic predictions of the LSTM and Neural ODE shown against the expected value of CVSFM.

E.5 Hyperparameter Guidance

The proposed CVFM framework introduces two primary hyperparameters governing the conditional coupling: the kernel bandwidth, σ_y, and the transport penalty, η. While our extensive ablations (Figures E.1, E.5, E.6) demonstrate that CVFM is remarkably robust to hyperparameter choice compared to unregularized baselines, we offer the following practical heuristics for their selection in new applications.

Kernel Bandwidth (σ_y): The bandwidth σ_y in the conditioning mismatch kernel, $\alpha(w) = \exp(-\|y_0 - y_1\|_2^2/2\sigma_y^2)$, defines the effective scale of local support over which conditional vector fields are aggregated.

- *Heuristic*: We recommend setting σ_y to approximately the **10th percentile** of Euclidean distances between randomly sampled conditioning pairs. This tighter bandwidth ensures the kernel focuses on the local support of the conditioning manifold, effectively filtering out disparate conditions while remaining robust to outliers.

- *Sensitivity*: As illustrated in Figure E.6 (Right), the method exhibits exceptional stability across bandwidths spanning several orders of magnitude (10^{-1} to 10^{1}). Extremely small values of σ_y approach the regime of exact matching (reducing effective sample size), while excessively large values approach the unregularized limit. The broad plateau of low objective target variance suggests that precise tuning is rarely necessary, provided σ_y restricts interaction to the local scale of the conditioning data.

Transport Penalty (η): The penalty η in the anisotropic ground cost (Eq. 10) biases the Optimal Transport solver to prefer couplings with matched conditioning variables ($y_0 \approx y_1$).

- *Heuristic*: We recommend setting η sufficiently high (e.g., $\eta \in [10, 100]$) to strongly penalize transport along the conditioning manifold, effectively acting as a soft constraint.
- *Interplay with CVFM*: In standard Conditional OT (COT-FM), performance is highly sensitive to η, as the solver must rigidly enforce conditional constraints to avoid mismatched pairings. However, CVFM relaxes this dependency. As shown in Figure E.5, the conditioning mismatch kernel $\alpha(w)$ effectively filters out high-cost pairings from the OT solve, maintaining low Wasserstein-2 error even when η is suboptimal. Consequently, users should prioritize a large enough η to guide the coarse coupling, relying on the kernel to handle local consistency.